Substorm evolution as revealed by THEMIS satellites and a global MHD simulation

Mostafa El-Alaoui,[1] Maha Ashour-Abdalla,[1,2] Raymond J. Walker,[1,3] Vahé Peroomian,[1] Robert L. Richard,[1] Vassilis Angelopoulos,[1,3] and Andrei Runov[1]

[1] The major substorm that occurred on 1 March 2008 had excellent spacecraft coverage by the THEMIS spacecraft in the magnetotail, GOES 11, and GOES 12 at geosynchronous orbit and Geotail in the dayside magnetosheath. A global magnetohydrodynamic simulation of this substorm, driven by Wind solar wind observations, accurately reproduced the magnetospheric observations. The simulation revealed the complexity of magnetotail dynamics during the substorm, in particular, in the near-Earth plasma sheet. Reconnection began prior to the substorm on closed field lines and a flux rope formed there. Around substorm onset, the simulation exhibited flow vortices near the locations of THEMIS P3 and P4, in agreement with observations at P3 and P4. These vortices were associated with a duskside neutral line that formed early in the substorm. Six minutes later, another neutral line formed on the dawnside of the tail. These neutral lines then merged to form a single large reconnection region that extended across the tail and greatly expanded the flux rope. The least active part of the tail was the region around midnight. Strong flows were seen in the observations and in the simulation during the two intensifications of this substorm; in particular, tailward flows were seen at THEMIS P1 and P2. Reconnection on closed field lines, vortices in the near-Earth region, a channel of strong tailward flow, and enhanced precipitation into the ionosphere all contributed to substorm development.

1. Introduction

[2] The magnetotail is the primary energy storage reservoir for magnetic substorms and the magnetotail current sheet is the location of the energy release processes that drive magnetic substorms. The two most important magnetotail regions for substorm development are the transition region from dipole to taillike magnetic fields [*Takahashi et al.*, 1987; *Lui et al.*, 1999; *Shiokawa et al.*, 1997] and the midtail location associated with near-Earth neutral line formation [e.g., *Baker et al.*, 1996]. The cause and effect relationship between the elements of the substorm process, a long-standing puzzle in the field is the subject of intense study with the advent of the THEMIS mission [*Angelopoulos*, 2008]. *Angelopoulos et al.* [2008] observed plasma sheet reconnection, well within the plasma sheet boundary [*Zhou et al.*, 2009], to occur less than 100 s prior to auroral onset

during several substorms, suggesting that plasma sheet reconnection may be responsible for the initiation of substorm energy release, i.e., in advance of the major substorm energization. *Lui et al.* [2008] reported on a substorm onset with subsequent intensifications, which did not initially involve lobe flux reconnection. The above results point to the fact that reconnection deep inside the plasma sheet may participate in early stages of substorms. The nature and evolution of this reconnection process early in the substorm process is poorly understood because of its localized character, and deserves attention because observational studies of substorm triggering are affected by localized currents and flows.

[3] In the near-Earth magnetosphere the initial substorm phase, the growth phase [*McPherron*, 1970], is characterized by strong taillike magnetic field distortions and energetic particle variations thought to result from a thinning and enhancement of the tail current sheet [*Kokubun and McPherron*, 1981; *Nagai*, 1982; *DeForest and McIlwain*, 1971; *Baker*, 1984]. The growth phase is also characterized by dramatically increased pressures in the plasma sheet [*Spence et al.*, 1989; *Kistler et al.*, 1992; *Lyons and Samson*, 1992]. The near-Earth behavior is usually described in terms of the substorm current wedge [*McPherron et al.*, 1973], in which the cross-tail current is reduced or disrupted by

[1]Institute of Geophysics and Planetary Physics, University of California, Los Angeles, California, USA.
[2]Department of Physics, University of California, Los Angeles, California, USA.
[3]Department of Earth and Space Sciences, University of California, Los Angeles, California, USA.

deviation of the current from the tail region to the Earth through the auroral ionosphere. This current deviation is accompanied by a dipolarization of the magnetic field in the near-Earth region that had been stretched during the preceding substorm growth phase [*McPherron*, 1979]. Observations suggest that the initial auroral brightening that signals the start of the substorm expansion phase maps to this near-tail region [*Frank and Sigwarth*, 2000, and references therein]. In the midtail, substorms are accompanied by strong flows which are often intermittent [e.g., *Angelopoulos et al.*, 1992, 1997] and evidently localized [*Ashour-Abdalla et al.*, 1999; *Yermolaev et al.*, 1999].

[4] The two major phenomenological models of the substorm can be distinguished by the different relationships between the processes in the two critical regions. In the near-Earth initiation or current disruption model, a physical process acting close to the Earth (-6 to $-15\ R_E$) [*Lui*, 1991, 1996] ultimately leads to strong flows in the midtail. In contrast, in the midtail initiation model, the substorm process begins at a downstream distance of -15 to $-30\ R_E$. In this model, magnetic reconnection in the near-Earth tail triggers the next phase of the substorm, the expansion phase [e.g., *Baker et al.*, 1996], and the ejection of a plasmoid or magnetic flux rope down the tail [*Hones et al.*, 1984]. Statistical studies indicate that reconnection frequently occurs between $-30\ R_E < x < -20\ R_E$ [*Nagai et al.*, 1998]. Supporters of this near-Earth neutral line model of substorms have generally assumed that the neutral line formation occurs in the late growth phase and that it may even cause substorm onset. Magnetohydrodynamic (MHD) simulations of substorms under ideal conditions are generally consistent with this model [e.g., *Birn and Hesse*, 1991; *Walker et al.*, 1993]. In the current disruption model [*Lui*, 1991] substorm onset and plasmoid formation and ejection are separate processes. *Lopez et al.* [1993] noted that dipolarization starts earthward of where the neutral line is supposed to form and they argue for a tailward propagating current disturbance. Birn and Hesse (see *Birn et al.* [1996] for a list of references), however, argue that the diversion of earthward flow from the near-Earth neutral line can provide the necessary current disruption and dipolarization.

[5] While tail reconnection is included in both substorm models, there is little agreement regarding just where in the tail the reconnection occurs and how this location affects the onset of the expansion phase. Both models have in common the formation of thin current sheets, magnetic reconnection, and the tailward progression of dipolarization occurring during substorms, but differ in other respects, in particular, the onset time of magnetic reconnection with respect to substorm expansion onset time.

[6] Determining the sequence of events in the magnetotail during an actual substorm is difficult. We never have sufficient spacecraft coverage to determine the complete response of the tail. Therefore, we have been studying substorms by using a combination of spacecraft observations and simulations of the magnetosphere to try to obtain a three-dimensional time-dependent view of the changes in the magnetosphere during a substorm. In this paper we present a case study of a substorm on 1 March 2008 which had exceptional coverage by spacecraft in the near-Earth magnetosphere. We use observations and a global MHD simulation to address questions about the onset of the substorm and its spatial dependence. In section 2 we briefly describe the MHD model. In section 3 we present an overview of the observations during this substorm. In section 4 we show that the MHD simulation realistically models the observations from the fleet of spacecraft in the magnetotail. We will quantify the individual comparisons using cross-correlation coefficients. Encouraged by this we use the simulation results (in section 5) to give us a picture of the changes in the entire magnetosphere during this substorm. Finally we discuss our results in section 6 and place them in the context with previous studies.

2. MHD Model

[7] Our coupled three-dimensional magnetohydrodynamic (MHD) magnetosphere-ionosphere code is based on a single fluid description of the interaction between the solar wind and Earth's magnetosphere. A detailed description of the MHD model can be found in the work by *Frank et al.* [1995], *Raeder et al.* [1998, 2001], and *El-Alaoui* [2001].

[8] In the MHD simulation, the total electric field includes convective and resistive terms, and is given by: $\mathbf{E} = -\mathbf{v} \times \mathbf{B} + \eta \mathbf{J}$, where v is the bulk flow velocity, B is the magnetic field, J is the current density, and η is the resistivity. Explicit resistivity is necessary in our code for reconnection to occur. The resistivity η in our code is defined by

$$\eta = \begin{cases} \alpha \mathrm{j}_1^2 & \text{if } \mathrm{j}_1 \geq \delta \\ 0 & \text{otherwise} \end{cases} \quad \text{where} \quad j_1 = \frac{|j|\Delta}{|B| + \varepsilon}$$

where j is the local current density, B is the local magnetic field, Δ is the grid spacing and ε is a very small number added to avoid division by zero. To avoid spurious dissipation we have a threshold $\delta = 0.65$ for the local normalized current density. This threshold is calibrated such that explicit resistivity is switched on only at a very few grid points in intense current sheets. Similar models based on current-driven instabilities have been used successfully in local MHD simulations [*Sato and Hayashi*, 1979]. The dimensions of the simulation box are 20 R_E in the sunward direction, 300 R_E along the tail, and 55 R_E in each transverse direction. With such a large simulation domain, all flows at the external boundaries are in the supermagnetosonic regime.

[9] The MHD equations are solved on a Cartesian computational grid that is computed prior to the run by using continuous functions to distribute the grid points in the simulation system. We can achieve high resolution in the central plasma sheet because in our case the MHD grid is computed prior to the run. The size of each grid cell is defined by three continuous functions that allow us to increase the grid resolution in regions of interest without excessively degrading the resolution in the rest of the simulation domain where a coarse resolution will not significantly affect the global processes and will preserve outgoing flow boundary conditions.

[10] The time step in the simulations is determined by the Courant condition $\tau = \Delta/V_A$ where Δ is the minimum grid spacing and V_A is the maximum Alfvén velocity in the
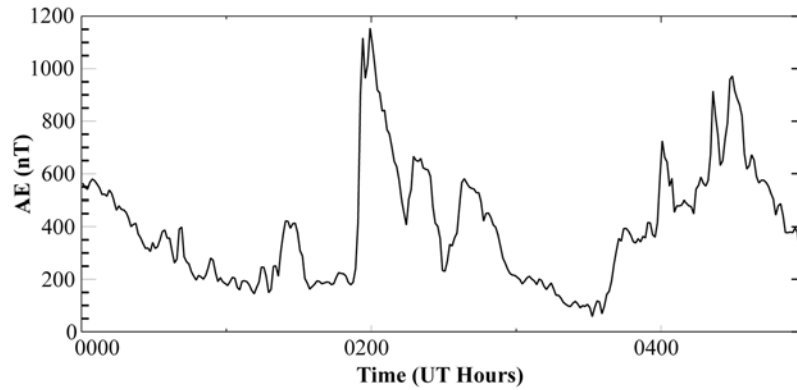
Figure 1. The AE index derived from THEMIS ground stations.

simulation domain (~4000 km/s near the Earth). The time step in these calculations ($T = 0.075$ s) is determined by the parameters near the inner boundary of the simulation.

3. Observations

[11] Between 0000 UT and 0500 UT on 1 March 2008 the magnetotail was in a disturbed state. The auroral electrojet (AE) index derived from THEMIS ground magnetometer stations shown in Figure 1 indicates that there were multiple activations during this interval. One minor activation that was identified as a pseudobreakup on the basis of all-sky camera observations began near 0148 UT and a second activation believed to be the main substorm onset began near 0155 UT [*Runov et al.*, 2008]. The THEMIS derived AE reached approximately 1200 nT during this substorm. Another substorm began around 0400 UT. The time interval between 0100 and 0220 UT will be the primary focus of this paper. During this interval, the THEMIS spacecraft were in a major conjunction on the duskside of the magnetotail. A total of nine spacecraft were sampling different regions of the magnetosphere and the Geotail satellite was in the dayside magnetosheath. Figure 2 shows the locations of the spacecraft that were in the magnetosphere projected onto the noon-midnight meridian plane (Figure 2, bottom) and the equatorial plane (Figure 2, top) in GSM coordinates, which will be used throughout this paper. Seven of these spacecraft, including the 5 THEMIS satellites, were on the duskside of the magnetosphere. Nominal positions for the bow shock and the magnetopause also are shown. Geosynchronous GOES 11 and GOES 12 were located at ~2000 LT and ~1600 LT, respectively. THEMIS P5 (A) was located inside geosynchronous orbit, while THEMIS P4 (E) and P3 (D) were located at 8 and 9.3 R_E downtail, respectively. THEMIS P2 (C) was located at $x \sim -17$ R_E and finally THEMIS P1 (B) was located at around 22.6 R_E downtail. The Cluster spacecraft were at high southern latitudes above the dawnside auroral zone.

[12] Geotail was located on the dayside at $x \sim 9.94$ R_E. Geotail's location in the magnetosheath allowed it to be used to confirm that the solar wind plasma and the interplanetary magnetic field (IMF) that WIND observed did, in fact, interact with the magnetosphere during the study interval and that these features were being represented

correctly in the input to the MHD simulation. This comparison is discussed in section 4.1.

[13] During the 0000–0500 UT time interval the Wind spacecraft was located about 198.0 R_E upstream of Earth in the dawn sector ($y = -40$ R_E) and below the ecliptic plane ($z = -38$ R_E) in GSM coordinates. An overview of the solar wind plasma and the IMF observed by Wind is shown in
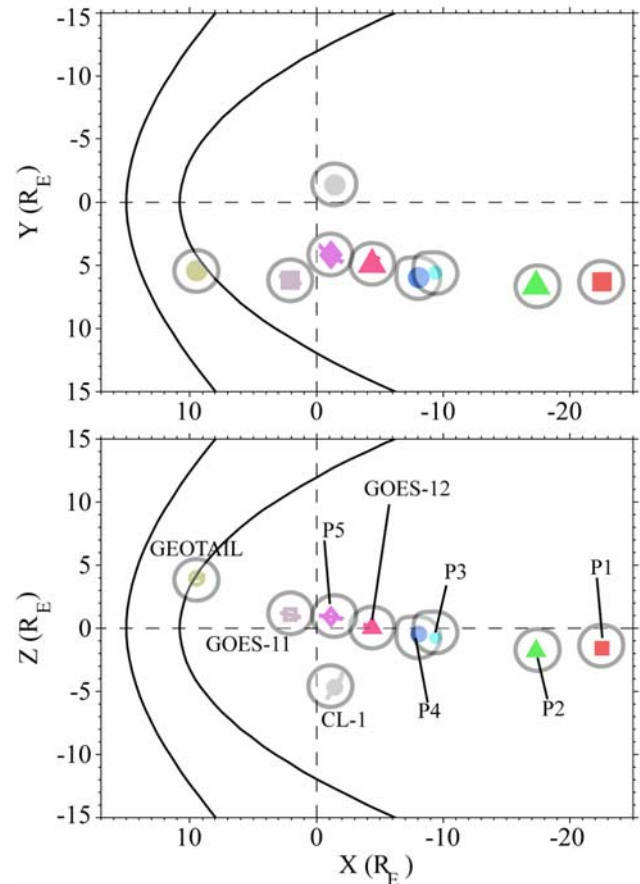

Figure 2. Projection of the spacecraft trajectories between 0130 and 0230 UT (with points marked at 0200 UT) (bottom) on the noon-midnight meridian plane and (top) on the equatorial plane.
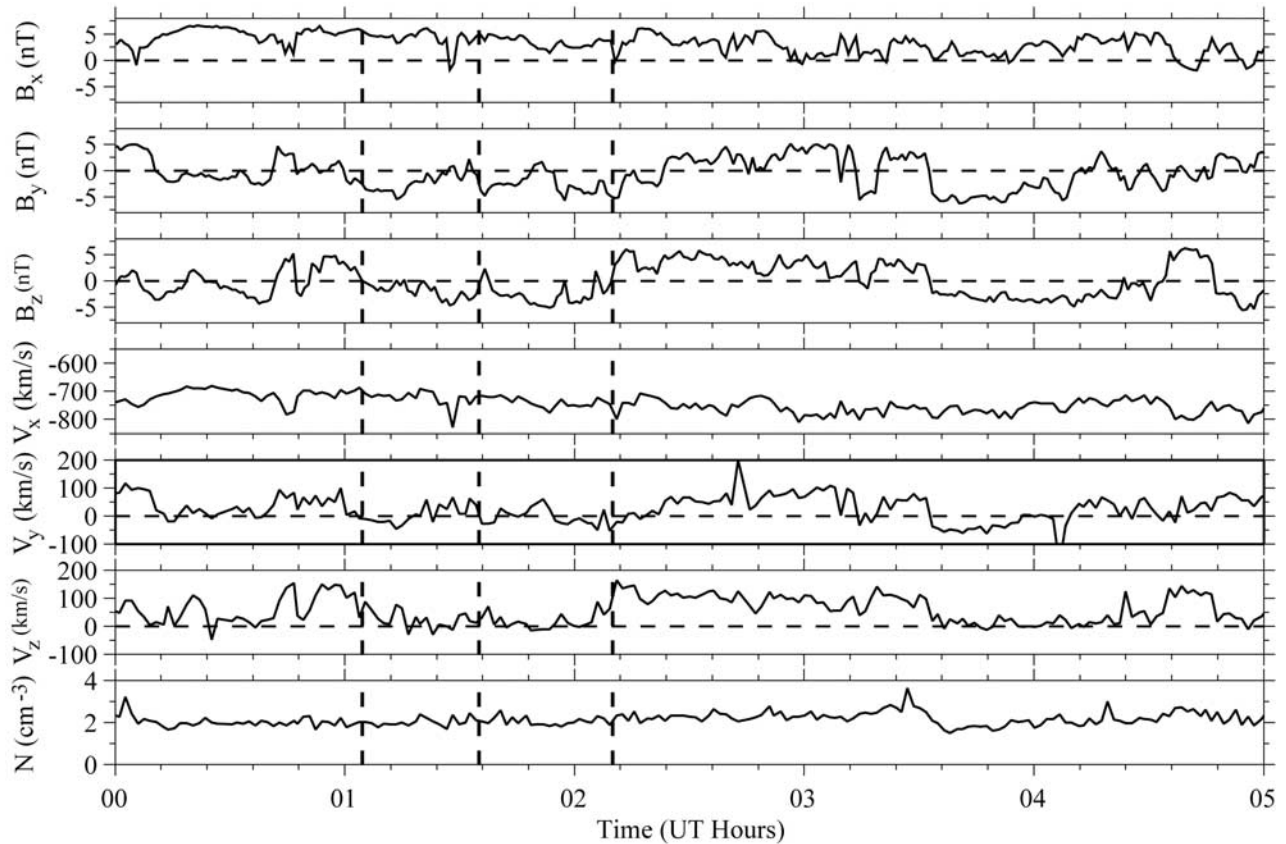
Figure 3. Solar wind parameters for 1 March 2008 measured by the Wind satellite. The Wind observations shown have been shifted by 28 min to account for the propagation time to the Earth's location. (first, second, and third panels) Magnetic field components, (fourth, fifth, and sixth panels) velocity components, and (last panel) the solar wind density are shown.

Figure 3. A time shift of 28 min has been applied to compensate for the time required for the solar wind to propagate from the Wind location to the MHD simulation's upstream boundary at $x = 25$ R_E. The first three panels of Figure 3 show the IMF, and the last four panels show the solar wind plasma velocity and density as a function of time. During this event the magnetosphere was subjected to a fast solar wind of low density, accompanied by a variable IMF. By about 0105 UT (first vertical dashed line in Figure 3) the IMF B_z component turned southward and continued drifting slowly southward until it reached a minimum of -5 nT around 0128 UT, while B_y was mainly directed dawnward. At 0134 UT (second vertical dashed line in Figure 3) the IMF B_z turned sharply northward for a very short time before turning southward for about 36 min. B_y remained mainly dawnward until the renewed southward IMF began at 0134 UT, when it turned duskward. At about 0210 UT (third vertical dashed line in Figure 3) the IMF B_z turned northward and remained so until 0334 UT. During this interval the IMF B_y turned duskward. The IMF B_x was fairly steady for the duration of the interval. The solar wind density was relatively low and very steady at just above 2 cm^{-3} during the whole interval. Meanwhile, the solar wind speed was high; it varied between ~ -700 km/s and -800 km/s, but because of the low density the resulting dynamic pressure was about 2 nPa. The V_y and V_z compo-

nents of the flow velocity reached 150 km/s which represented about 20% of the total speed.

4. Comparisons With in Situ Magnetotail Observations

[14] Two approaches have been taken in carrying out comparisons between MHD simulation results and space-craft observations. In the first, synthetic auroral emissions are derived from the simulation results and compared with auroral images [*Fedder and Lyon*, 1995]. In the second approach, time series of magnetic field and plasma parameters from the simulations are compared with those measured by spacecraft in the magnetosphere. These approaches have been used successfully to study the dynamics of the magnetospheric boundary [*Frank et al.*, 1995] and the plasma sheet during substorm intervals [*Lopez et al.*, 1998; *Raeder et al.*, 1998, 2001; *Winglee et al.*, 1998; *Ashour-Abdalla et al.*, 1999, 2000; *El-Alaoui*, 2001; *El-Alaoui et al.*, 2004, 2008]. In these studies, the simulation results showed general agreement with the spacecraft observations. The data-simulation comparisons show the aspects of an event that are correctly represented in the MHD simulation allowing us to place them in a global dynamic context by using the simulation results. We first carry out a comparison in which we use the simulated electron energy
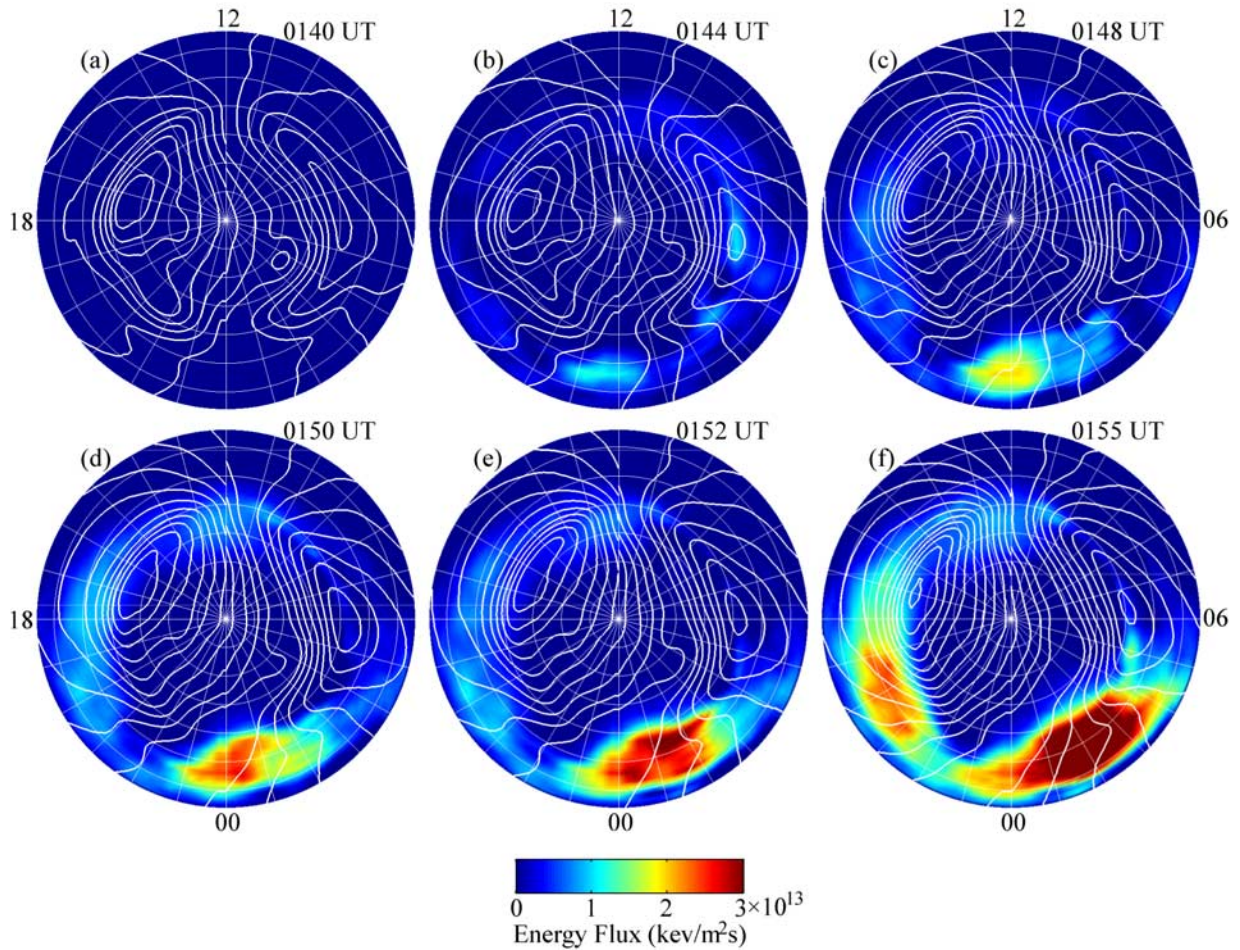
Figure 4. Change in energy flux into the ionosphere from a baseline at 0140 UT as a function of time. Superimposed on the energy flux are isocontours of electric potential.

flux into the ionosphere as a proxy for the aurora to check the substorm timing from the MHD simulation. In sections 4.1–4.3 we apply the second approach by comparing time series of the magnetic field component and plasma data from the MHD simulations with those measured by spacecraft in the magnetosheath and magnetosphere.

[15] There are two components to the energy flux into the ionosphere in the simulation due to particle precipitation. The first component represents discrete electron precipitation [*Knight*, 1973] and is given by

$$F_E = \frac{\sqrt{2\pi \mathrm{m}_e k T_e}}{e^2 n_e} \max\left(0, -j_\parallel\right) \cdot j_\parallel \qquad (1)$$

where n_e, T_e and m_e are the electron density, temperature and mass at the ionosphere boundary while $j_\parallel$ is the parallel current density mapped along dipole field lines into the ionosphere from the inner boundary of the simulation.

[16] The second contribution is diffuse precipitation and is parameterized by

$$F_E = n_e k T_e \sqrt{\frac{k T_e}{2\pi m_e}} \qquad (2)$$

where, n_e and T_e are the magnetospheric electron density and temperature.

[17] *Runov et al.* [2008] used all sky camera observations from the THEMIS array to identify both minor and major onsets of this substorm. *Runov et al.* [2008, Table 1] identify a minor onset starting at 0148 UT and a major onset at 0155 UT.

[18] Figure 4 shows the change in energy flux from a baseline at 0140 UT (Figure 4a) at a selection of times. Superimposed on the energy flux are electric potential isocontours. The flux has increased moderately around midnight by 0144 UT. The flux near midnight has increased greatly by 0148 UT, the time of the minor onset (pseudo-breakup) identified by *Runov et al.* [2008]. The energy flux continued to increase gradually until a major increase occurred just dawnward of midnight at 0152 UT. That increase was followed by an even larger increase at 0155 UT which extended duskward of midnight.

[19] The time history of the electron precipitation was consistent with the THEMIS all-sky camera and AE observations. During the first substorm THEMIS AE (Figure 1) reached a much higher maximum (above 1000 nT) close to the onset time, while the second substorm showed a more moderate rise to near 400 nT near onset followed by a slow increase to ~800 nT. Prior to the second substorm the
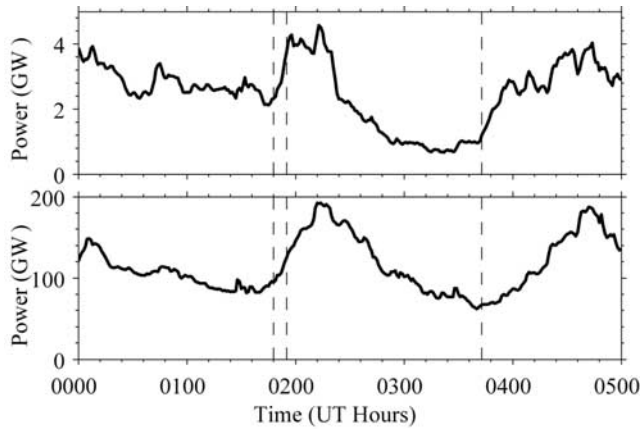
Figure 5. Power deposited into the ionosphere. (top) The power associated with discrete aurora. (bottom) The power associated with diffuse aurora.

activity level reflected in the AE index (Figure 1) was lower (75 nT) than for the first substorm (200 nT). To illustrate this we show (Figure 5) the time histories of the power deposited in the ionosphere because of discrete (equation (1)) and diffuse (equation (2)) precipitation. The simulated ionospheric power showed a similar pattern for the diffuse aurora power for both substorms. However, the discrete aurora showed significant differences between the two events. While the diffuse aurora dominated the total power (Figure 5, bottom), the discrete auroral power (Figure 5, top) increased more rapidly between 0148 UT and 0155 UT (indicated by the vertical dashed lines). A second major substorm onset is also indicated by a vertical dashed line at 0343 UT. The first substorm had a much more dramatic peak in the discrete power compared to the second substorm that occurred near 0343 UT. The discrete auroral power is much higher prior to the first substorm and the first substorm shows a sudden power increase at onset followed by a slow decay. The second substorm shows a continued increase after the onset. Both substorms eventually reached a power level of nearly 200 GW in the simulation.

4.1. Geotail and MHD

[20] During this event the Geotail spacecraft moved from the magnetosheath to the magnetosphere (Figure 6). The red lines in Figure 6 show the observed magnetic field (B_x, B_y, B_z) components and the last panel shows the magnitude of the field measured by the Geotail magnetometer [*Kokubun et al.*, 1994] versus time. The magnetic field data are 64-s averages. The time series from the MHD simulation at the location of Geotail is plotted with black lines. To quantify the comparisons between the Geotail observations and the MHD simulation results for the magnetic field we have computed cross-correlation coefficients for each magnetic field component during the interval from 0115 UT to 0245 UT. The cross-correlation coefficients were 0.94 for B_x, 0.15 for B_y and 0.83 for B_z. When we applied a 5 min backward shift in the MHD results the cross-correlation coefficients became 0.92 for B_x, 0.44 for B_y and 0.81 for B_z.

[21] Around 0212 UT Geotail crossed the magnetopause. This can be seen (Figure 6) in the magnetic field. B_x changed from positive to negative, B_y turned from dawn-

ward to duskward and B_z turned from southward to northward and the total field doubled from its value prior to 0212 UT. The MHD model agreed well with observations, in particular the crossing of the magnetopause around 0212 UT, except that the B_y predicted by MHD after the magnetopause crossing remained positive for some time. The timing for the magnetopause crossing is complicated in both the MHD simulation and the GEOTAIL observations because of substructures within the magnetopause. For instance, the crossing times inferred from different magnetic field components differ by a few minutes. The magnetopause structure in the observations features a twisting in the y and z components of the magnetic field that is different in the simulation, but the change in the magnitude of the magnetic field during the crossing is reproduced. The simulation is therefore reproducing the crossing time within the resolution imposed by the magnetopause structure. The magnetopause crossing in the MHD simulation is further illustrated in Figure 7. Figure 7 (left) shows color contours of the z component of the magnetic field at the Geotail location ($y \sim 5.3\ R_E$) to illustrate the jump in the field observed around 0212 UT. Figure 7 (right) shows the total current at the same location to illustrate the position of the bow shock and magnetopause. Between 0140 UT and 0220 UT Geotail moved from (9.8, 5.2, 3.8) R_E close to the bow shock to (9.0, 5.6, 4.1) R_E within the magnetopause current layer (Figure 7, right). As Figure 7 (left) indicates, by 0210 UT the IMF B_z was northward (warm colors on scale) and the magnetosheath field was strongly northward, which is consistent with the Geotail observations. It is
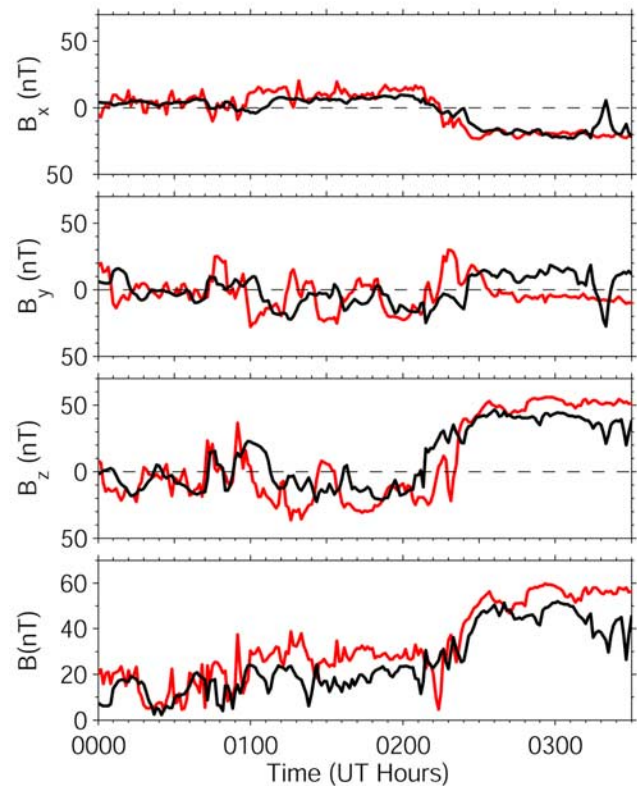

Figure 6. Comparison of Geotail magnetic field observations (red lines) with simulation results (black lines) at the Geotail location.
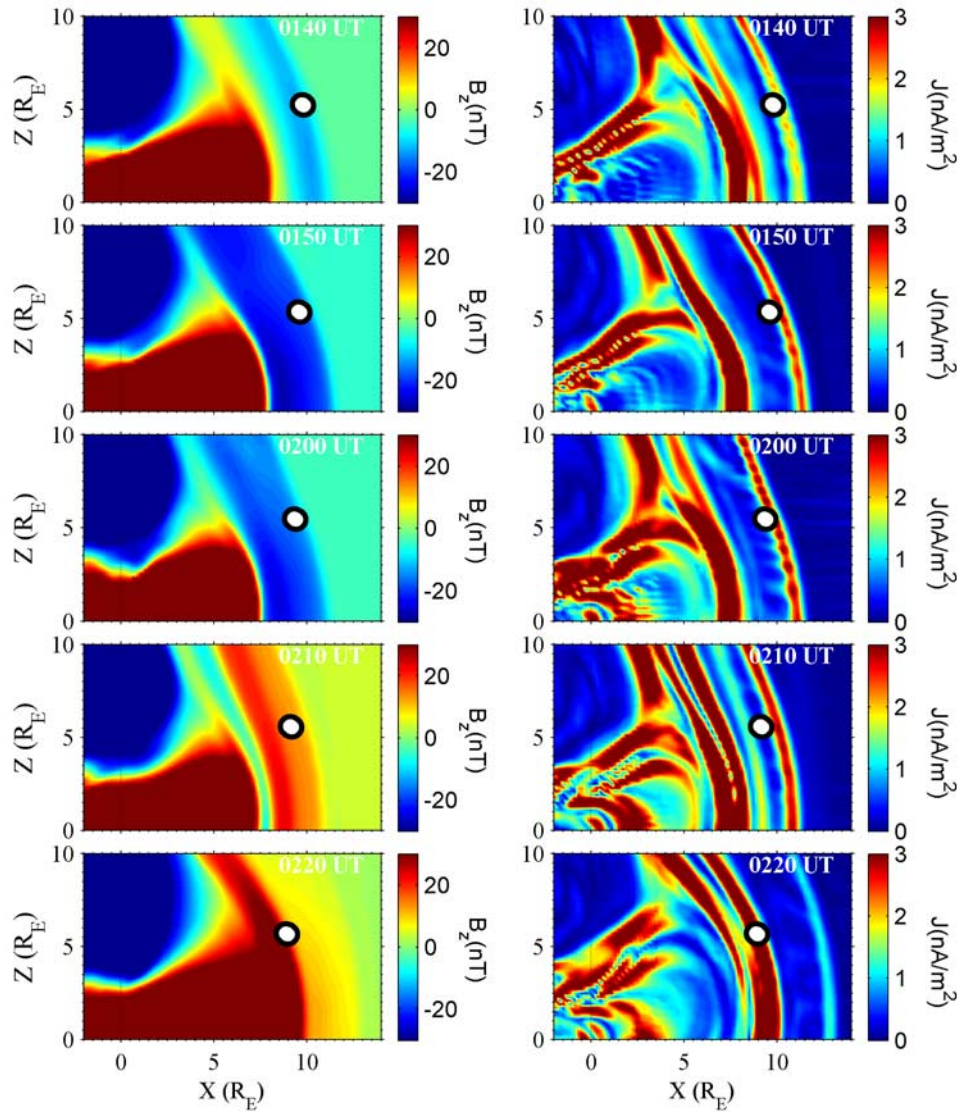
Figure 7. Cross sections of the MHD simulation results at the Geotail y location (5.3 R_E). Shown are (left) the magnetic field component B_z and (right) the total current density from 0140 to 0220 UT.

interesting to note that at 0210 UT when B_z was becoming strongly positive, a new structure formed in the magneto-sheath current density (Figure 7, right) just earthward of Geotail. In the next 10 min this new structure merged with the outward moving magnetopause currents (0220 UT). These results support the use of WIND data to determine the solar wind and magnetosheath conditions during this substorm.

4.2. GOES 11, GOES 12, and MHD

[22] Figure 8 (left) shows a comparison between the observed magnetic field from GOES 11 with the MHD simulation, and the comparison of the GOES 12 magnetic field and the MHD results is shown in Figure 8 (right). GOES 11 was near 2000 local time while GOES 12 was near 1600 local time. For both spacecraft the MHD results for B_x were less than the measured values (first panels). However, the MHD simulation reproduced several varia-tions in the B_y and B_z components measured by GOES 11 and GOES 12. In particular, the simulation reproduced the

variations seen around the onset of the substorm at 0155 UT. At this time, the B_z component decreased in magnitude at the GOES 11 position. A similar decrease was also seen at GOES 12. The simulation reproduced the overall variability observed, with the exception of underestimating (more negative) B_x. This may be because the MHD simulation did not include a ring current model. The cross-correlation coefficients for GOES 11 (GOES 12) were 0.51 (-0.57) for B_x 0.07 (0.77) for B_y, and 0.68 (0.69) for B_z and with a 5 min lag in the MHD results the coefficients are 0.65 (-0.66) for B_x 0.25 (0.88) for B_y, and 0.41 (0.47) for B_z. For the 36 h prior to this substorm, the Dst index hovered between -25 nT and -30 nT, possibly affecting the results in the near-Earth region. Alternatively, the good agreement for the total field suggests that the primary problem is a rotation of the field, possibly due to the use of a fixed dipole tilt (taken at 0300 UT). The most prominent features related to the substorm seen at the GOES satellites are drops in B_z around 0154 UT at GOES 12 and around 0202 UT at GOES 11. These changes in B_z were seen in both the simulation and
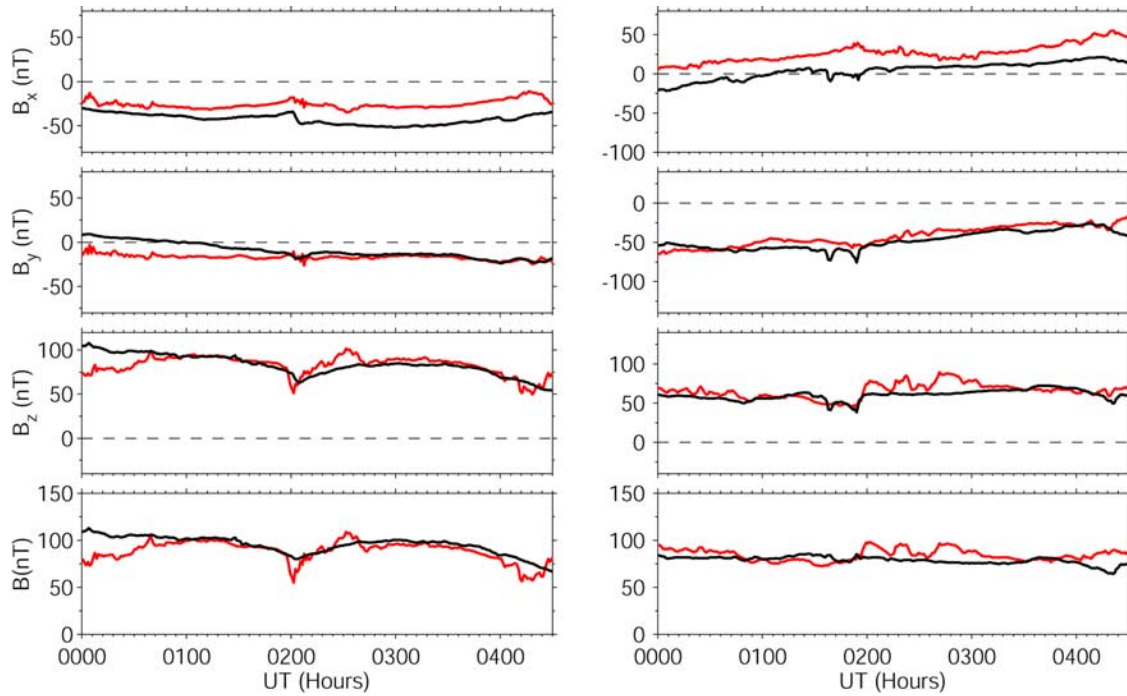
Figure 8. Comparisons of time series from (left) GOES 11 and (right) GOES 12 with MHD simulation results. The magnetic field component data are shown as red lines, and the MHD simulation results are shown as black lines.

the observations although as usual some details, such as exact timing, are different. These changes were due to the spacecraft passing through localized current systems. GOES 11 passed through a region of sheared magnetic field which was accompanied by strong gradients in B_x and B_y associated with a current in the z and x directions (not shown). A downward-field-aligned current existed near the magnetic shear. At GOES 12 the decrease in B_z was associated with a strong gradient in B_z in the longitudinal direction (Figure 9, left). The gradient at GOES 12 was related to a local current system as we show in Figure 9 (right).
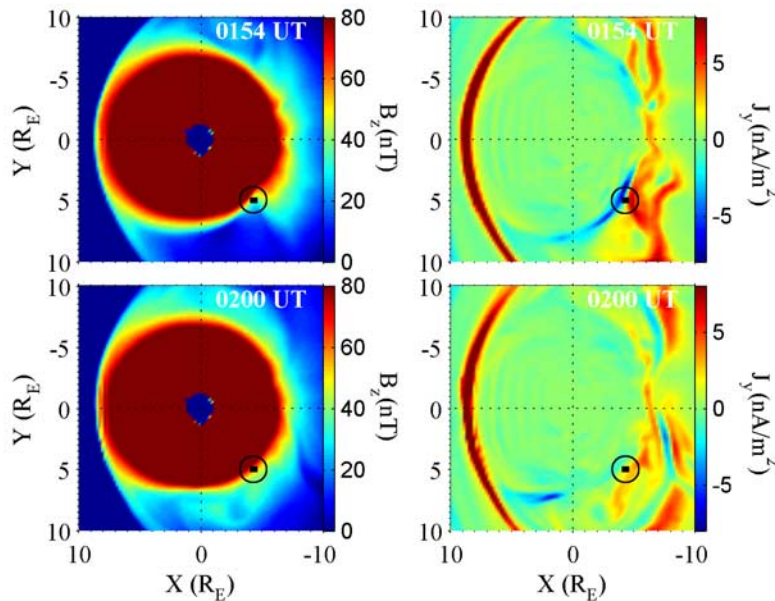

Figure 9. Changes in current and magnetic field at GOES 12 near substorm onset. (right) Cuts at the z location of GOES 12 show that a longitudinal gradient in Bz existed near 0154 UT but not at 0200 UT. The gradient seen at 0154 UT was accompanied by a localized current system; (left) the y component of the current is shown.
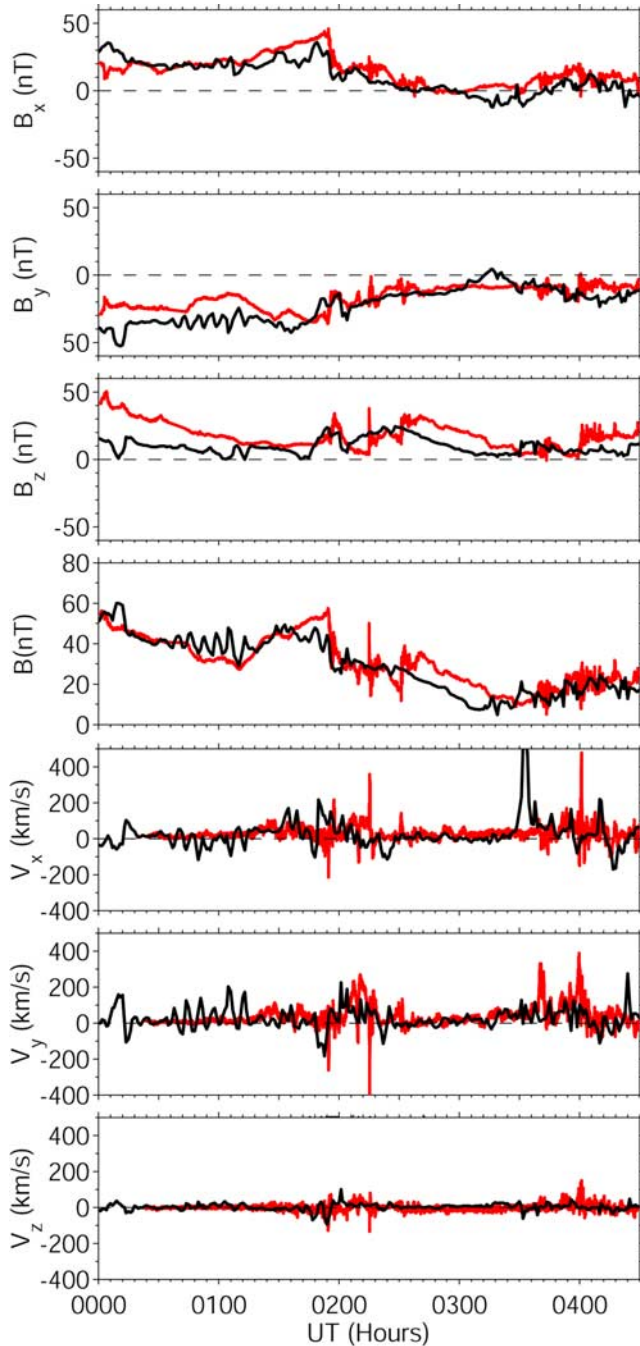
Figure 10. A comparison of (first four panels) observed magnetic field time series from THEMIS P4 and (last three panels) flow velocity components with simulation results. The data are shown in red, and the MHD simulation results are shown in black.

4.3. THEMIS Observations and MHD

[23] At the substorm onset the THEMIS spacecraft were in a major conjunction close to the magnetotail current sheet. Recall that the first intensification, identified as a pseudobreakup by *Runov et al.* [2008], occurred around 0148 UT and the second or main intensification occurred around 0155 UT. Comparisons between the different THEMIS spacecraft and the MHD simulation will be

presented in this section. Later, this comparison will help us to put the observations in a global context. Our discussion will proceed from THEMIS P4 outward to the more distant spacecraft in the tail region. THEMIS P5 (not shown) was inside geosynchronous orbit where the dipole is dominant.

[24] To quantify the comparison between the THEMIS data and the MHD simulation results for the magnetic field we have computed, for each THEMIS spacecraft, a cross-correlation coefficient for each magnetic field component for the interval from 0115 UT to 0245 UT. For the cross-correlation calculations the THEMIS data were averaged over 1 min to match the times of the MHD output. These cross-correlation coefficients were computed for both no time shift and for a 5 min forward shift to the simulation results, which usually improved the fit.

4.3.1. Comparison With THEMIS P4 and P3

[25] Because THEMIS P3 (D) and P4 (E) were close together during the interval we have combined the comparisons between these spacecraft and the simulations into one section. Around 0155 UT THEMIS P4 was located in the near-Earth tail at (-8.05 R_E, 5.97 R_E, -0.43 R_E). THEMIS P3 was located slightly tailward at (-9.35 R_E, 5.61 R_E, -0.74 R_E) at 0155. Comparisons between THEMIS P4, magnetic field components and magnitude, and the MHD results are shown in the first four panels of Figure 10. The magnetic field observations are at 3-s intervals from 0000 UT to 0430 UT; the black lines indicate the results from the MHD model obtained at 60-s intervals. The THEMIS P4 observations can be organized most easily by the x component of the magnetic field (B_x). The sign and magnitude of B_x measured by THEMIS P4 indicates that the spacecraft was located in the northern plasma sheet and crossed the current sheet for a very short time around 0244 UT. Afterwards, the spacecraft remained close to the neutral sheet for a long time. Overall, the comparison shows that the observations agree well with the simulation. The MHD simulation captured the broad trend as well as several key features in the observations. The cross-correlation coefficients were 0.93 for B_x 0.81 for B_y, and 0.50 for B_z. With the 5 min shift in the MHD results the cross-correlation coefficients became 0.89 for B_x 0.88 for B_y, and 0.70 for B_z. THEMIS P3 sees development similar to THEMIS P4 (Figure 11). Again the agreement between the simulation and data was good. The cross-correlation coefficients were 0.93 for B_x 0.70 for B_y, and 0.24 for B_z. With the 5 min shift in the MHD results the cross-correlation coefficients became 0.86 for B_x 0.88 for B_y, and 0.48 for B_z. At the time of onset around 0155 UT, the predicted B_x component of the magnetic field from the MHD simulation showed a sharp decrease consistent with the THEMIS P4 and P3 measurements. At the same time (0155 UT), an increase can be seen in the B_z component, corresponding to a dipolarization, in both the observations and the simulations. The y component of the magnetic field drifted slowly from strongly dawnward to dawnward with a magnitude of around 10 nT. The changes and the magnitude of the B_y component of the magnetic field observed by THEMIS P4 were well reproduced by the simulation.

[26] The last three panels of Figure 10 show the three velocity components V_x, V_y, and V_z from the ESA and SST particle instruments on P4 versus time. The resolution of the
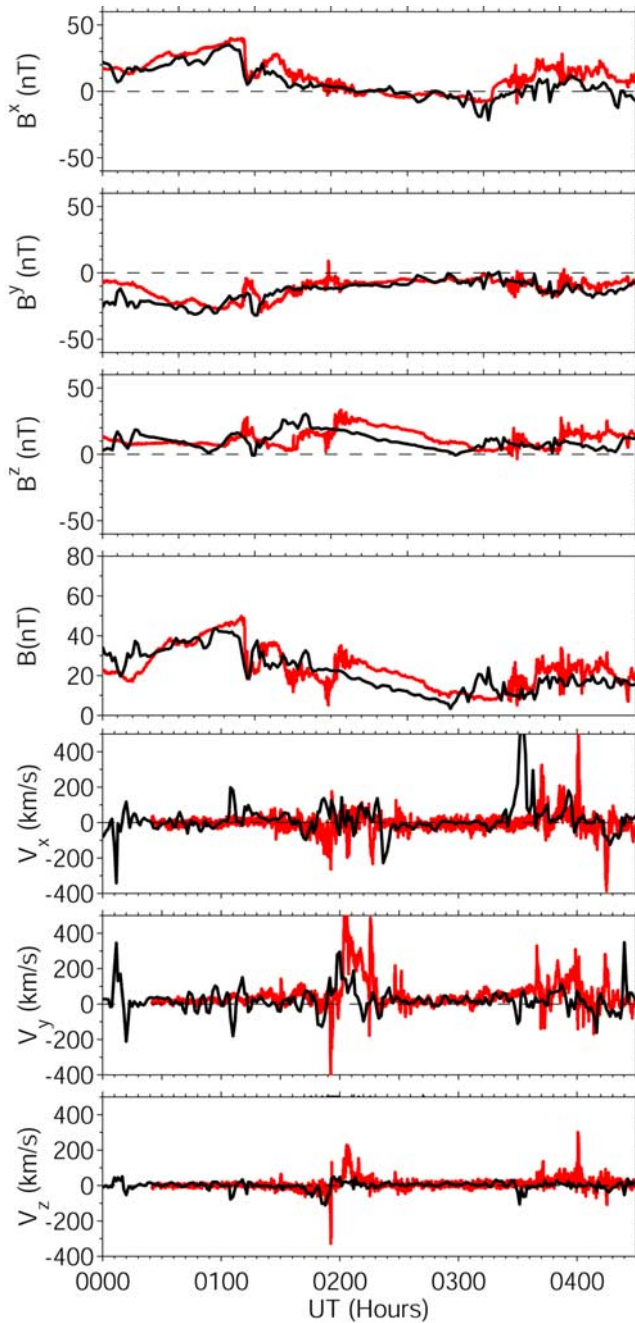
Figure 11. A comparison of observed magnetic field and flow velocity component time series from THEMIS P3 with simulation results in the same format as Figure 10.

plasma moments is 3 s. The MHD model results show reasonable agreement with observations. The interval around 0200 UT is characterized by enhanced flows, first dawnward and then duskward, in both the simulation and observations. The drop in B_x at THEMIS P4 around 0155 UT was accompanied by the maximum tailward flow seen during the interval (Figure 10). This tailward flow corresponds to a weaker tailward flow in the simulation about 5 min earlier. In fact, the sequence of flow reversals starting around 0154 UT in the observations, that is, tailward then earthward then tailward, is also seen in the simulation. They match in timing when the 5 min delay is included. The very

high earthward flow prior to 0155 UT, which is not reflected in the observations, in the simulation was much weaker only 0.25 R_E further from the neutral sheet in the simulation. The sequence of tailward and earthward flows accompanying the drop in B_x at 0155 UT at P3 (Figure 11) was similar to that at THEMIS P4. At P3, the observed V_y component was even larger than was seen at P4, with both the dawnward and duskward flows reaching 400 km/s. The simulated flows were also high but not as high as the observations (Figure 11), reaching only about 200 km/s dawnward and 350 km/s duskward. The agreement between observations and MHD results is reasonably good given the limitations of the three-dimensional structure of the solar wind measurements and the inherent limitations of the model, in particular the relatively coarse resolution in the grid, which was 0.2 R_E in the y and z direction. The overall pattern of the MHD V_x, V_y and V_z components agreed very well with observations though reproducing all the rapid fluctuations in velocity are beyond the capabilities of the model.

[27] To illustrate the processes occurring in the simulation in the vicinity of P3 and P4, Figure 12 displays a series of cross sections parallel to the y-z plane at the x location of P3 near the time of the dropout and the dipolarization seen by THEMIS P3. These snapshots show the x component of the magnetic field at six key times between 0149 UT and 0159 UT. Figure 12 is displayed in GSM coordinates and is viewed from the direction of the Sun. The open circle in each panel indicates the position of the THEMIS P3 spacecraft. The black contour levels are located where B_x is near zero to emphasize the changes in its sign. Around 0149 UT, one minute after the first intensification, a small wave-like structure developed just below and dawnward of P3 position. This structure moved duskward, becoming more pronounced around 0155 UT, and engulfed the THE-MIS P3 position. This structure then widened and moved duskward. In the simulation, the magnetic field changes seen by P3 were surprisingly localized.

4.3.2. Comparison With THEMIS P2

[28] THEMIS P2 (C) was located in the tail at $(-17.34\ R_E,$ $6.65\ R_E, -1.78\ R_E)$ at 0155 UT. The calculated and observed magnetic fields at the position of the THEMIS P2 spacecraft are shown in the first four panels of Figure 13. The simulated B_x (black curve in Figure 13 (first panel)) tracks the THEMIS P2 observations reasonably well until about 0200 UT. Beginning at ∼0200 UT the observed B_x sharply increased from −25 nT (in the southern hemisphere) to 15 nT (in the northern hemisphere) within 4 min. After this B_x became negative and remained so for more than an hour. The MHD model did not reproduce the rapid variation in the current sheet after 0200 UT. However, the simulation did a good job in reproducing several other structures seen in the B_x component, and the cross-correlation coefficient was 0.62. The simulation reproduced the changes as well as the magnitude of the B_y component and the cross-correlation coefficient for this component was 0.59. However, the simulation did only a fair job of reproducing the observations during the interval as a whole. The simulation as well as THEMIS P2 observations showed a negative B_z around the time of onset and the simulation did a reasonably good job of reproducing the overall trends in this component of the magnetic field. The cross-correlation coefficient for B_z was only 0.26, although including the 5 min shift as previously
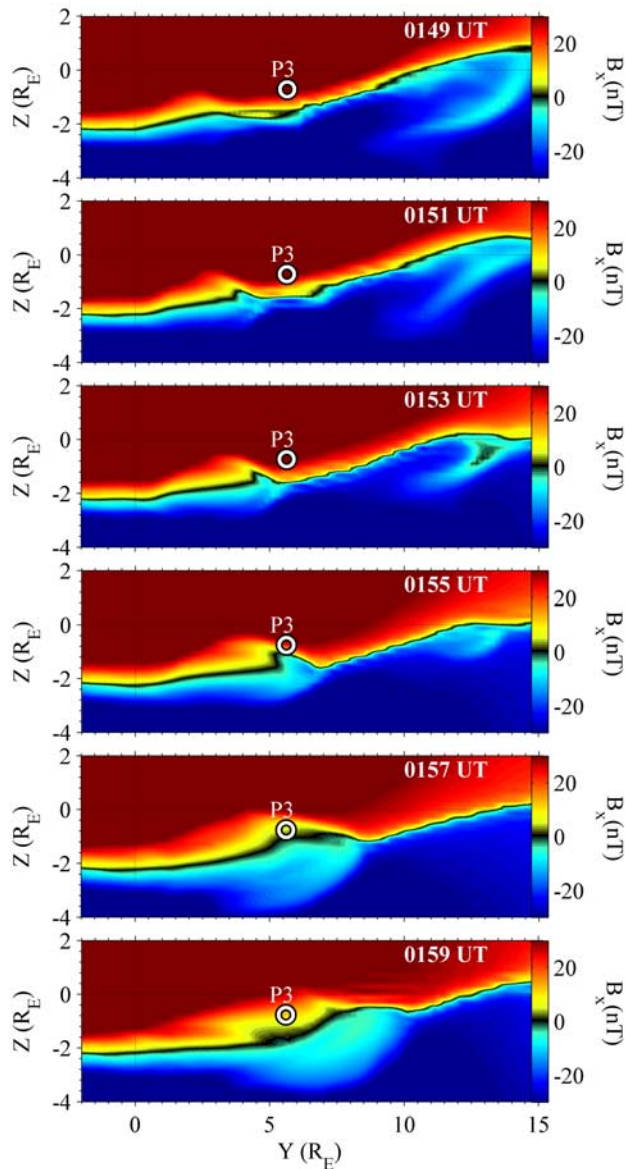
Figure 12. Cross sections of the *x* component of magnetic field in the *y-z* plane at the location of P3 ($x \sim -9.3$ R_E) from the simulation at different times. The open circle in each panel indicates the position of the THEMIS P3 spacecraft.

scale fluctuations that are beyond the capabilities of the model.

4.3.3. Comparison With THEMIS P1

[29] THEMIS P1 (B) was the furthest spacecraft from Earth and at 0155 UT was located in the midtail region at (-22.59 R_E, 6.3 R_E, -1.59 R_E). Figure 14 shows a comparison between THEMIS P1 observations and the MHD simulation. The simulation did not do as good job of reproducing the variations seen in the observations at P1 as it did at other spacecraft. Both the observations and the
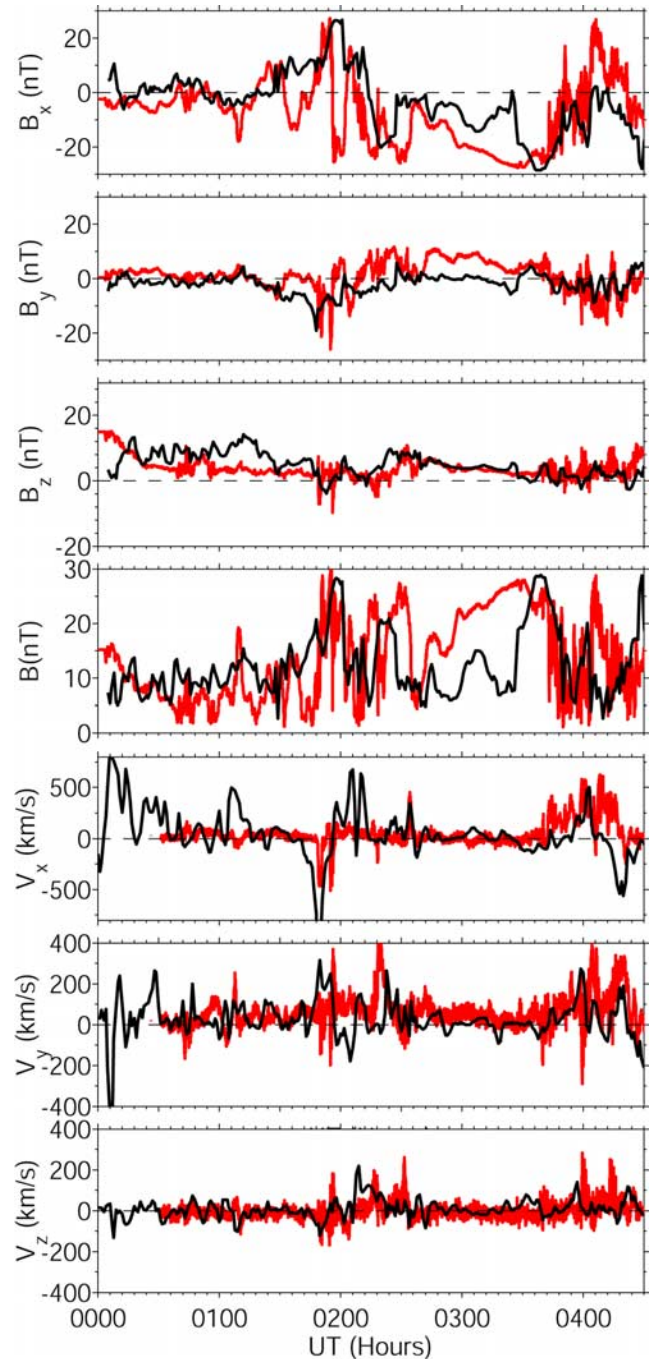

Figure 13. A comparison of observed magnetic field and flow velocity component time series from THEMIS P2 with simulation results in the same format as Figure 10.

this coefficient improved to 0.45. The agreement between the computed and observed magnetic fields gives us some confidence that the overall global configuration of the magnetotail that the model provides is valid. The last three panels of Figure 13 show the three velocity components V_x, V_y and V_z calculated from the ESA and SST observations on P2. The interval around 0200 UT is characterized by strong flows, first tailward and then earthward, in both the simulation and observations. The simulation shows a higher-speed flow that starts a few minutes earlier than the observations from THEMIS P2. The simulation does a fair job of reproducing changes in the V_y component similar in magnitude and direction to those observed by P2. Overall, the agreement between the observations and MHD results is reasonably good, but the flow velocity had many small-

Figure 14. A comparison of observed magnetic field and flow velocity component time series from THEMIS P1 with simulation results in the same format as Figure 10.
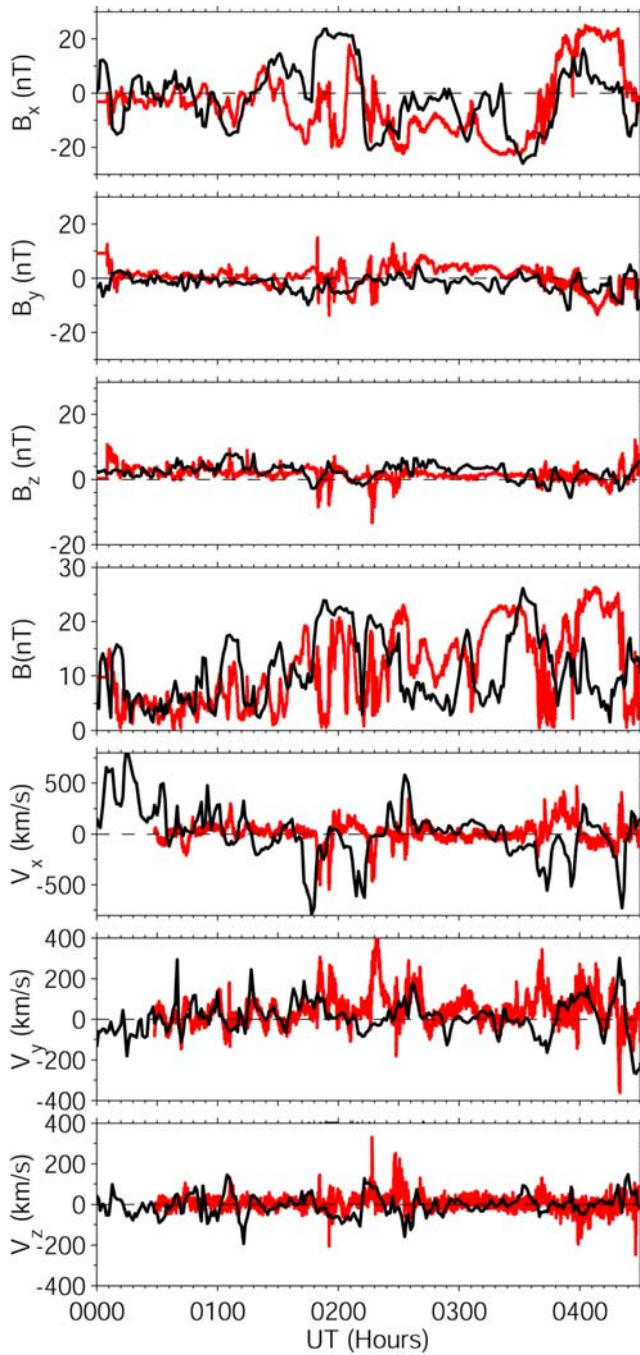
simulations showed large and rapid variations in the magnetic field indicating multiple current sheet crossings. The cross correlations for the magnetic field component were 0.32 for B_x 0.26 for B_y, and 0.16 for B_z. With the 5 min shift in the MHD results the cross-correlation coefficients became 0.31 for B_x 0.24 for B_y, and 0.42 for B_z. Although the simulation did not reproduce all of the details of these variations, it does have the overall variability and captures some of the specific variations. Both THEMIS P1 and THEMIS P2 observed intense tailward streaming around the time of onset that was also seen in the simulation. The

simulation exhibited the two southward B_z excursions, one around the time of onset of the substorm at 0155 UT and the second around 0212 UT. The observations showed sudden southward dips around the same times.

5. Global Configuration of the Magnetotail From an MHD Perspective

[30] It is difficult to determine the configuration and the dynamics of the magnetotail from single-point measurements and we turn to the MHD simulation to understand the development of the substorm. Overall we found that the magnetotail spacecraft were sampling localized, albeit important, processes. Because a combination of dipole tilt and finite IMF B_x and B_y yields a magnetospheric configuration without a good symmetry plane, we have developed a technique to display parameters at the three-dimensional current sheet in a two-dimensional format [*Ashour-Abdalla et al.*, 2002; *Peroomian et al.*, 2007]. We constructed a surface that approximated the current sheet location, determined the desired MHD quantity (e.g., velocity) there and then projected the results onto the $z = 0$ plane. The surface where the plasma pressure reaches a maximum value can be used as a proxy for the current sheet. This is more convenient than using the current itself which must be computed from the curl of the MHD magnetic field. In regions outside the magnetotail, for instance the dayside and the magnetosheath, the surface is set to a default value of $z = 0$. In complex cases where there are multiple local pressure maxima, a variation of the algorithm can choose which of several local maxima gives the most continuous overall solution. To extend the surface to the near-Earth and dayside regions, the surface at which $\vec{B} \cdot \vec{r} = 0$ can be used, where $\vec{B}$ is the magnetic field and $\vec{r}$ is a vector from the center of the Earth to a given point. There may be a discontinuity between the near-Earth and magnetotail solutions in that case.

[31] This technique is used in Figure 15, where three MHD parameters are superimposed. The color contours give the north-south component of the magnetic field at the surface and the black isocontours show the plasma thermal pressure. Finally, the white arrows give the x and y components of the flow velocity. Surfaces are plotted at times between 0142 UT and 0155 UT. The open circles in each plot indicate the positions of the four THEMIS spacecraft projected onto the maximum pressure plane. We have plotted the magnetic topology in Figures 15b, 15d, 15f, and 15h: with blue for closed magnetic field lines, yellow for open field lines, and red for field lines that are not connected to the Earth. Figure 15a, at 0142 UT, shows a time well before the first intensification at 0148 UT. Small regions of tailward flow associated with negative B_z have appeared duskward and dawnward of the THEMIS P3 and P4 spacecraft. These small regions can be seen in B_z as the transition from warm colors to cold colors and by the flow reversals from earthward to tailward at $x \sim -11\ R_E$. At this time the simulation indicated that reconnection was starting earthward of P1 and P2 but the tailward flows and southward B_z had not yet reached these satellites. By 0148 UT (Figure 15c), the region of tailward flow and southward B_z was still mostly duskward of P3 and P4 but P1 and P2 were embedded in the tailward flows. At 0142 UT and 0148 UT
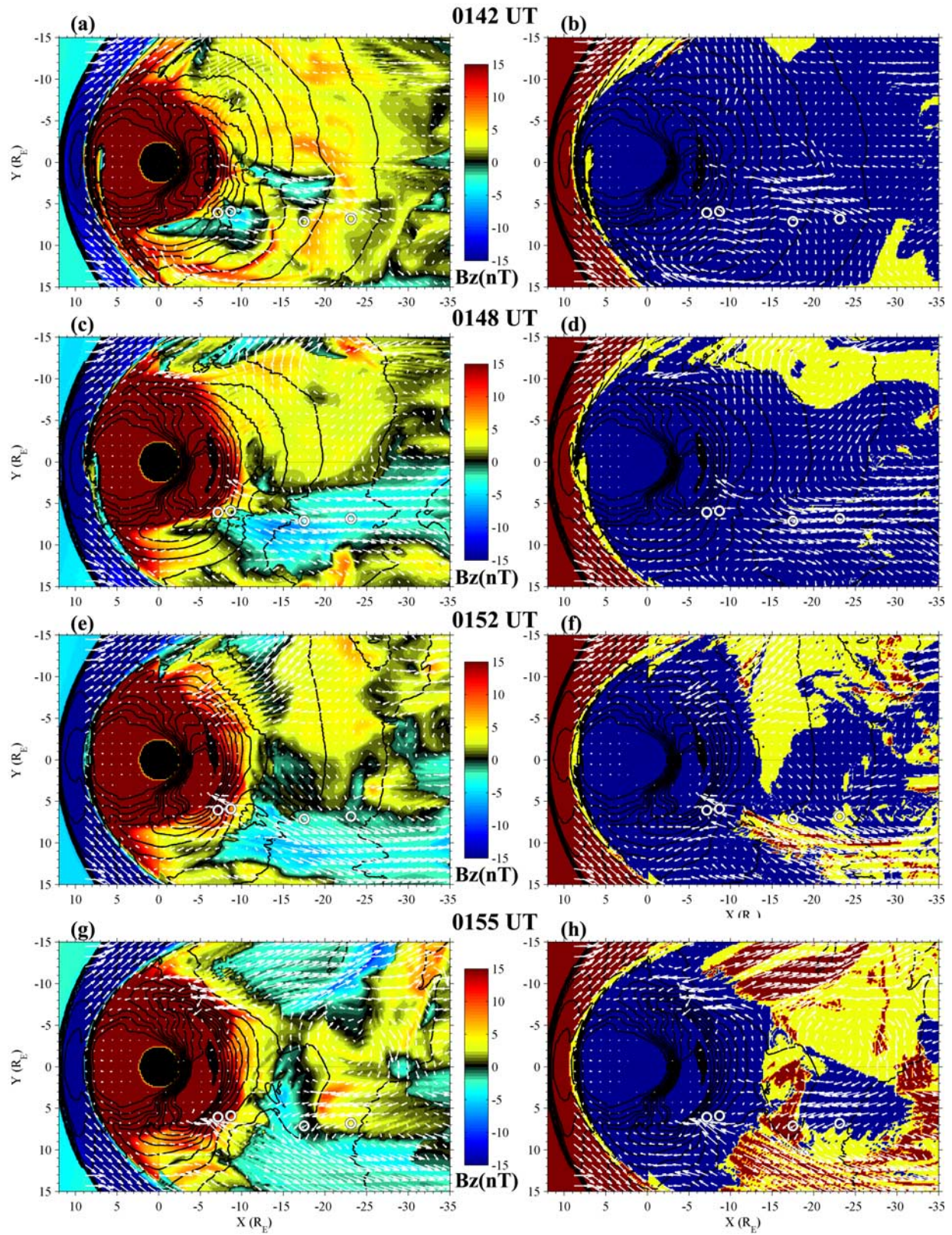
Figure 15. (a, c, e, and g) Three MHD parameters on the maximum pressure surface are superimposed. The color contours give the z component of the magnetic field, and the black isocontours show the plasma thermal pressure. The white arrows give the flow velocity on the surface. The open circles in each plot indicate the positions of four THEMIS spacecraft projected onto the maximum pressure surface. (b, d, f, and h) Magnetic topology is indicated: blue is for closed magnetic field lines, yellow is for open field lines, and red is for IMF field lines.
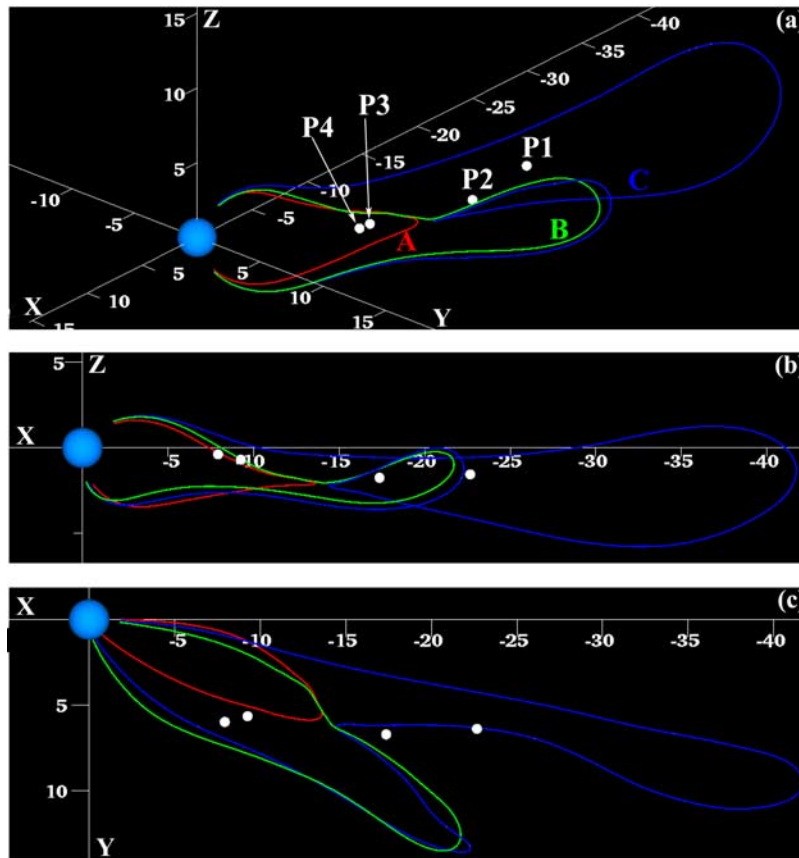
Figure 16. Three field lines, at 0148 UT, originating from a region bounded in x from -13.3 to -14.7 R_E and in y from 5.8 and 6.1 R_E. (a) A 3-D perspective, (b) a view from the duskside, and (c) a view from above.

(Figures 15b and 15d), the tail was dominated by closed field lines. This means that the reconnection identified in the near-Earth region at 0142 UT and 0148 UT was on closed field lines. A new neutral line that led to a growing region of open field lines appeared at about 0148 UT (Figure 15c). By 0152 UT (Figure 15f) the field lines tailward of the neutral line were either open or unconnected field lines.

[32] To illustrate the presence of reconnection on closed field lines at 0148 UT we show (in Figure 16) three views of three magnetic field lines at this time. Field line A (red) is a stretched tail field line that crosses the magnetotail current sheet near $x = -13$ R_E, $y = 6$ R_E, and $z = -2$ R_E, where it has a sharp bend. Field line B (green) is close to field line A north of the current sheet but tailward of the sharp bend in field line A they deviate and the two field lines are located far apart in the south. Field B crosses the current sheet near $x = -14$ R_E, $y = 6$ R_E, and $z = -2$ R_E. Viewed from the side (Figure 16b) the tailward part of this field line resembles a flux rope in the process of being pinched off and it has a considerable offset in the cross tail direction because of a strong y component to the magnetic field. Field line C (blue) has a sharp curvature just tailward of and in the opposite sense to the strongly curved part of field line A. This pair of field lines is the result of reconnection on field lines resembling field line B. Field line C closely follows field line B in the southern hemisphere, but has reconnected and formed a flux rope-like loop. The pattern of tailward flows on closed field seen by THEMIS P3 and P4 as well as in the

simulation has been observed and discussed in other event studies [*Ashour-Abdalla et al.*, 2002; *Walker et al.*, 2006]. These papers attributes the tailward flows on closed field lines to a combination of changes in the ionospheric precipitation and the resulting conductance combined with changes in pressure gradients in the inner plasma sheet.

[33] At the main substorm onset (0155 UT (Figure 15g)) the pattern of reconnection was complex. The strongest reconnection was on the duskside, duskward of P3 and P4, but P3 and P4 still saw a northward magnetic field and weak earthward flows. At this time, reconnection at the dawnside neutral line intensified (Figure 15e) and strong reconnection driven flow covered a wide azimuthal range in the dawn quadrant. This location mapped to the high auroral zone energy flux observed at 0155 UT on the dawnside of midnight (Figure 4). Regions with open and unconnected field lines extended all the way across the tail at 0155 UT (Figure 15g), leaving a large isolated area of closed field lines tailward, in the vicinity of P1 and P2. As the substorm evolved, the dawnside neutral line moved across the tail so that by 0202 UT (not shown) it extended most of the way across the tail. It also moved tailward and could be found on the duskside between P1 and P2. By 0202 UT P2, P3 and P4 were all on closed field lines while P1 was on unconnected field lines.

[34] As can be seen in Figure 15, the field and plasma configurations near P3 and P4 are complex. The neutral line near the THEMIS spacecraft moved a long way and there
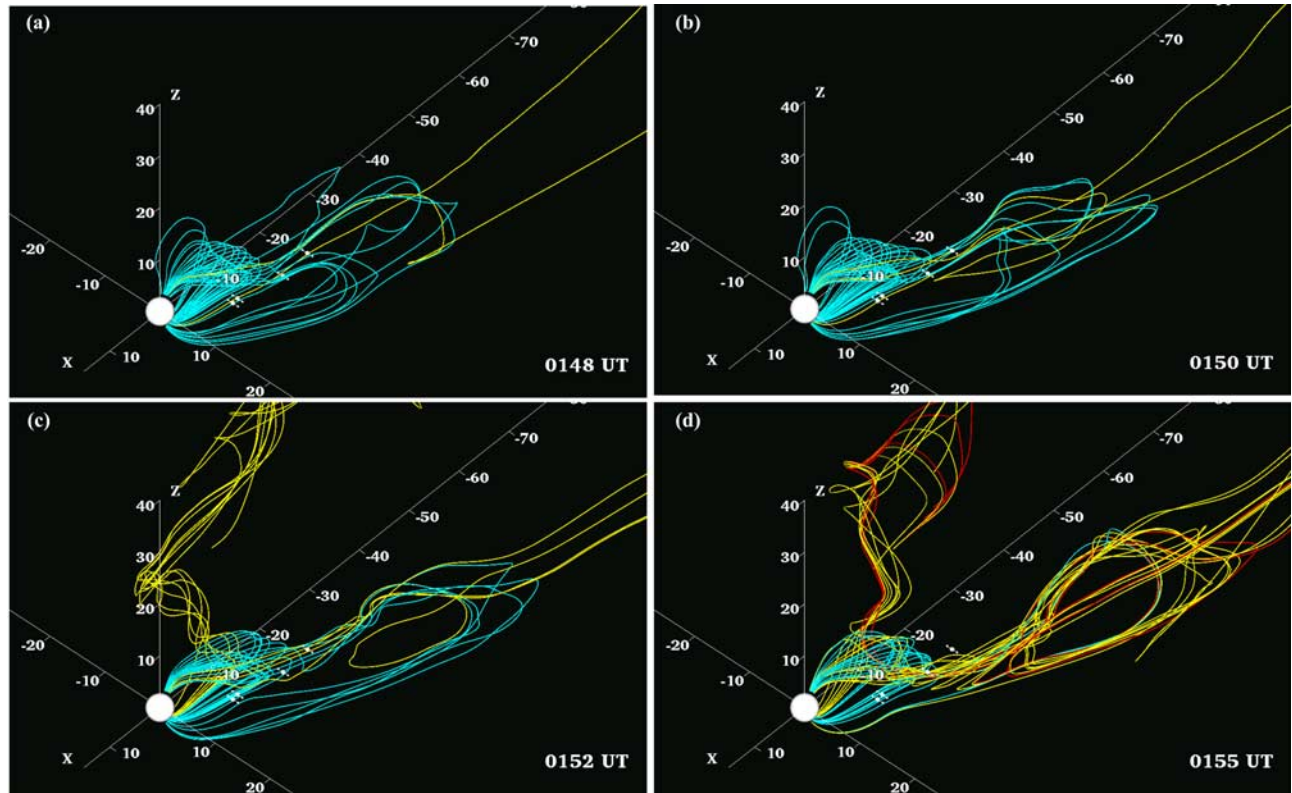
Figure 17. Field lines starting in a plane just tailward of P3 and P4. Closed field lines are blue, open field lines are yellow, and IMF field lines are red.

were regions of both IMF and closed field lines in the near Earth tail. The complexity of the field line configuration results from localized changes in magnetotail reconnection and the formation of a flux rope. The development of the flux rope is illustrated by displaying magnetic field lines in Figure 17. The field lines shown were started in a plane just tailward of P3 and P4. Closed field lines are blue, open field lines are yellow, and unconnected field lines are red. At the time of the first intensification (0148 UT (Figure 17a)), most of the field lines were closed. At 0150 UT and 0152 UT (Figures 17b and 17c) a flux rope existed in the closed field line region. This is caused by reconnection near P3 and P4 on closed field lines (Figure 16). Nearer substorm onset (0154 UT and 0155 UT (Figure 17d)), the flux rope has evolved into a large structure on the duskside and reconnection on open field lines was occurring. The region nearer midnight, however, was still dominated by closed field lines. This draping of closed field lines over the flux rope near midnight can still be seen at 0156 UT (not shown).

[35] Recall the good agreement between the simulation and observations for the dawn-dusk component of the flow velocity at THEMIS P3 and P4 locations for the interval around 0200 UT. This interval was characterized by enhanced flows, first dawnward and then duskward, in both the simulation and observations by P3 and P4 as shown in Figures 10 and 11. To illustrate the dynamics seen in the flow pattern at the P3 and P4 locations we have plotted, in Figure 18, B_z and flow vectors at the maximum pressure surface at six times. We focus on a small region of the tail 10 R_E in x by 10 R_E in y, to emphasize the structuring in the

flow. At 0148 UT (Figure 18a) the flows near P3 and P4 (shown as white circles) are earthward. By 0150 UT (Figure 18b) a vortex has formed dawnward of P3 and P4 that included a channel of rapid, predominantly earthward flow near the spacecraft. This vortex is associated with closed field line reconnection visible as a flow reversal in Figure 18a that extended from around $x = -11$ R_E in and $y = 7$ R_E to about $x = -5$ R_E and $y = 10$ R_E. This reconnection region moved tailward over the next few minutes (Figures 18b and 18c). At 0150 UT P4 was embedded in the earthward flow and two minutes later P3 was also in the flow (Figure 18c). The strong flow channel was duskward of P3 by 0154 UT and it was located in the duskward flow of the flow vortex. The movement of the flow channel and vortex relative to the spacecraft gave the V_y signatures observed by P3 and P4 (Figures 10 and 11). The twisted field line (line C) in Figure 16 is associated with this vortex. The initial slow duskward motion in the vortex was eventually blocked by the outward flow coming from the near-Earth neutral line at around 0148 UT (Figure 18a). Similar vorticity in the transition region between the midtail and the near-Earth (dominated) region has been seen in global MHD simulations [*White et al.*, 2001; *Ashour-Abdalla et al.*, 2002; *Walker et al.*, 2006] and inferred from ISEE observations in *Hones et al.* 1978 and 1981. The vortices in the work by *Hones et al.* [1978, 1981] and *White et al.* [2001] were attributed to flow shear while these in the work by *Ashour-Abdalla et al.* [2002] and *Walker et al.* [2006] were attributed to localized reconnection and flow braking.

[36] Flows that originated from a region around 15 R_E downtail split around $x = -10$ R_E and $y = 4$ R_E into two
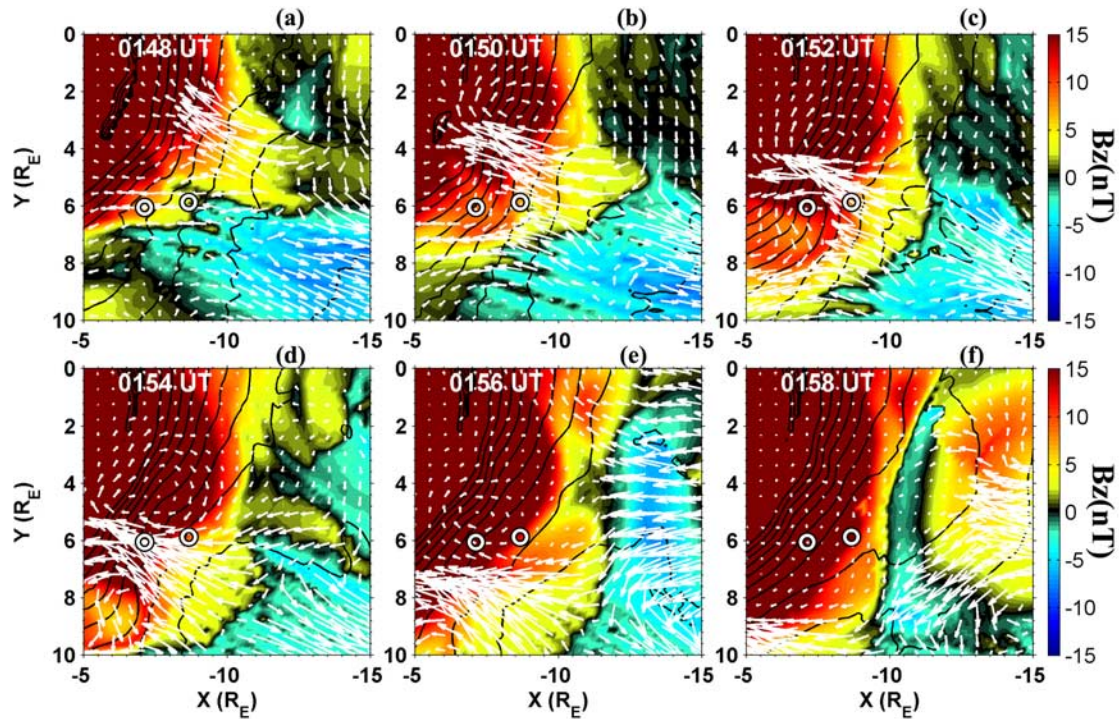
Figure 18. Three MHD parameters, as in Figure 15, are superimposed on the maximum pressure surface at six times.

parts, one directed dawnward and another directed dusk-ward. Later, at 0158 UT, the vortex seen on the duskside expanded in y but diminished substantially in intensity as can be seen in Figure 18f. The sequence of earthward flow followed by vortices formation (Figure 18) is similar to that reported by *El-Alaoui* [2001], *Ashour-Abdalla et al.* [2002] and *Walker et al.* [2006]. As suggested by *Ashour-Abdalla et al.* [2002], two mechanisms work together to cause the flow reversal. As the plasma moves earthward ionospheric precipitation increases and so does the Pedersen conductiv-ity. If the ionospheric conductance is too high, the magne-tosphere is unable to provide enough field aligned current to maintain the full cross magnetosphere potential across the ionosphere [*Coroniti and Kennel*, 1973]. When the earth-

ward magnetospheric convection is much larger than the rate at which the ionosphere can return flux to the dayside the earthward convection stops [*Walker et al.*, 2006]. However, the ionospheric line tying alone cannot reverse the flow direction. The earthward plasma pressure gradient in the near-Earth tail can both slow the plasma and reverse it. Figure 19 shows the change in thermal pressure from a baseline at 0148 UT (Figure 19, left) as a function of time. Superimposed on the thermal pressure are flow vectors. As the earthward convection proceeded, the pressure in the inner plasma sheet increased rapidly and then the flow reversed. This is consistent with the pressure gradient driving the flow reversal.
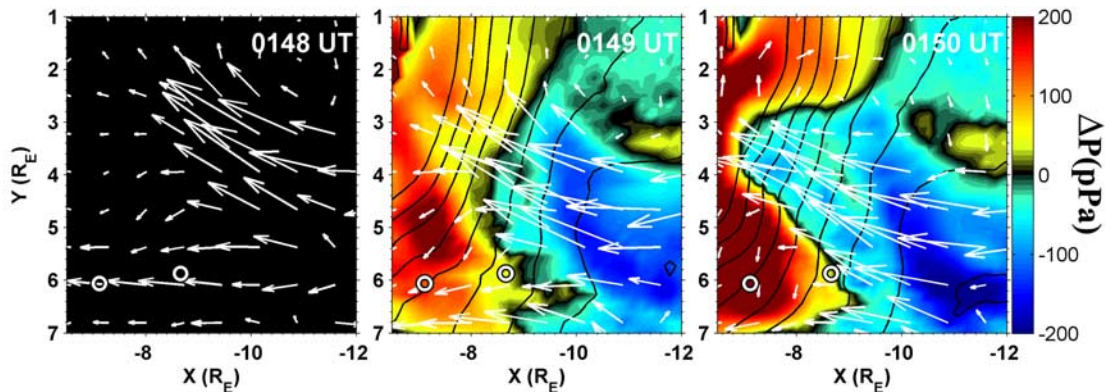

Figure 19. The color shading gives the change in thermal pressure from a baseline at 0148 UT as a function of time on the maximum pressure surface. The white arrows give the flow velocity. The black isocontours show the pressure. The open circles in each plot indicate the positions of two THEMIS spacecraft projected onto the surface.

[37] The second substorm, with onset around 0343 UT (Figure 1), had both similarities and differences that are apparent in both the observations and the simulation results. Near 0320 UT, prior to the onset of the second substorm, the MHD simulation results showed the formation of a pair of tailward flow channels reminiscent of that seen in Figure 15a. The flow pattern prior to onset had a weaker vortex structures (not shown) than seen in the first substorm.

6. Discussion and Conclusions

[38] A total of nine spacecraft were available during this event: the 5 THEMIS spacecraft in a major conjunction on the duskside, as well as GOES 11, GOES 12 and Geotail. Solar wind and interplanetary magnetic field data from Wind were available to drive the simulation. Detailed examinations of the THEMIS and all-sky camera observations were presented by *Runov et al.* [2008]. During the substorm, a series of intensifications followed a change to a predominantly southward IMF. The simulation did a very good job of reproducing several of the variations seen in the observed magnetic field components and plasma flow during this substorm event. The MHD simulation presented us with a very complex picture of the magnetosphere during this substorm. In the simulation, substorm dynamics were driven by reconnection in the near-Earth tail. However, the configuration was far from a simple neutral line across the tail. Reconnection was localized in azimuth. Both observations [e.g., *Yermolaev et al.*, 1999] and a previous global MHD substorm simulation [*Ashour-Abdalla et al.*, 1999] have indicated that, at least during some substorms, reconnection can be limited to local regions of the magnetotail. In addition, observational [*Sergeev et al.*, 1995, 1996] and theoretical [*Chang*, 1999] analyses suggest that small regions of localized reconnection may be common in the magnetotail. This paper provides evidence that such localized reconnection in the geomagnetic tail can explain the flows and magnetic field changes in the magnetotail observed by the THEMIS spacecraft.

[39] During this substorm, a neutral line was found on the duskside around 0142 UT (Figure 15). By 0148 UT neutral lines were present on both the dawnside and the duskside, but not near midnight. Eventually, by substorm onset around 0155 UT, reconnection extended across the tail and reconnection moved onto lobe field lines on both the dawnside and the duskside but remained on closed field lines near midnight. During the course of the event, the neutral line moved tailward. In particular, at the main substorm onset (0155 UT) the neutral line near THEMIS was located between P1 and P2.

[40] At the beginning of the first onset or pseudobreakup at 0148 UT, the simulation showed that reconnection on closed field lines was occurring tailward of THEMIS P3 and P4 but earthward of THEMIS P1 and P2. This reconnection process began several minutes earlier, duskward of THEMIS P3 and P4 and led to strong tailward flows at THEMIS P1 and P2. These tailward flows were observed by THEMIS P1 and P2. The tailward flow in the simulation first decreased and then increased, and the same behavior was found in the observations. Between 0148 UT and 0200 UT, the flow pattern revealed a vortex in the near-Earth plasma sheet that was observed at THEMIS P3 and P4. Several distinct

vortices formed in the tail as shown in Figures 15, 18, and 19. For instance, at 0152 UT in Figure 18 there is a clockwise vortex located at $2 R_E < y < 5 R_E$ and a counterclockwise vortex located at $6 R_E < y < 8 R_E$. Additional vortices can be found near P1 and P2 (Figure 15). A number of simulation studies have modeled large-scale vortices in the magnetotail [*Walker et al.*, 1998, 2006; *Ashour-Abdalla et al.*, 1999, 2002; *White et al.*, 2001; *El-Alaoui*, 2001]. *White et al.* [2001] found large-scale vortices in simulations with both northward and southward IMF as well as a simulation without an IMF. *Ashour-Abdalla et al.* [2002] and *Walker et al.* [2006] found large-scale vortices in event simulations during prolonged intervals with southward IMF. *El-Alaoui* [2001] found that during a substorm event in the near Earth plasma sheet ($x \approx -12 R_E$) the flow pattern revealed two vortices and that the flow pattern was associated with the redirection of part of the cross-tail current into the ionosphere. The redirection of the current around the intensification seemed to be related to a splitting of the flows into channels around two vortices. *Ashour-Abdalla et al.* [2002] and *Walker et al.* [2006] have suggested that vorticity in the tail is controlled by a combination of earthward pressure gradients and ionospheric Pedersen conductance.

[41] The MHD simulation of this event captured the main features of the substorm and compares convincingly well with the different spacecraft in the tail, in particular the THEMIS satellites. There are two paradigms for describing substorm onset, the near-Earth neutral line model, and the current disruption model. Our simulation results contain observational aspects of each of these paradigms. In our simulation, the substorm dynamics were driven by the evolution of magnetic reconnection, as in the near-Earth neutral line model [e.g., *Baker et al.*, 1996]. However, the reconnection responsible for the substorm started in a localized region on the duskside of the magnetotail on closed field lines. Strong reconnection did not occur near midnight until late in the substorm, when a neutral line extending across the tail was established. Another important feature in this substorm event consisted of flow vortices and flux ropes moving tailward. The near-Earth neutral line model also predicts flux pileup in the near-Earth region [*Hesse and Birn*, 1991] because of the braking of fast flows. This feature was not seen in our simulations around midnight. *Lui et al.* [1988] described the rapid north-south variations in the magnetic field in the near-Earth region as a current disruption event and further described the region as consisting of intertwined field lines. Our simulation clearly shows the presence of flux ropes and intertwined field lines in the near-Earth region, on closed field lines, where the current disruption is purported to occur.

References

Angelopoulos, V. (2008), The THEMIS mission, *Space Sci. Rev.*, *141*(1–4), 5–34, doi:10.1007/s11214-008-9336-1.

Angelopoulos, V., W. Baumjohann, C. F. Kennel, F. V. Coroniti, M. G. Kivelson, R. Pellat, R. J. Walker, H. Lühr, and G. Paschmann (1992), Bursty bulk flows in the inner central plasma sheet, *J. Geophys. Res.*, *97*, 4027–4039, doi:10.1029/91JA02701.

Angelopoulos, V., et al. (1997), Magnetotail flow bursts: Association to global magnetospheric circulation, relationship to ionospheric activity and direct evidence for localization, *Geophys. Res. Lett.*, *24*, 2271–2274, doi:10.1029/97GL02355.

Angelopoulos, V., et al. (2008), Tail reconnection triggering substorm onset, *Science*, *321*, 931–935, doi:10.1126/science.1160495.

Ashour-Abdalla, M., M. El-Alaoui, V. Peroomian, R. J. Walker, L. M. Zelenyi, L. A. Frank, and W. R. Paterson (1999), Localized reconnection and substorm onset on Dec. 22, 1996, *Geophys. Res. Lett.*, *26*, 3545–3548, doi:10.1029/1999GL003630.

Ashour-Abdalla, M., M. El-Alaoui, V. Peroomian, R. J. Walker, J. Raeder, L. A. Frank, and W. R. Paterson (2000), The origin of the near-Earth plasma population during a substorm on November 24, 1996, *J. Geophys. Res.*, *105*, 2589–2605, doi:10.1029/1999JA900389.

Ashour-Abdalla, M., M. El-Alaoui, F. V. Coroniti, R. J. Walker, and V. Peroomian (2002), A new convection state at substorm onset: Results from an MHD study, *Geophys. Res. Lett.*, *29*(20), 1965, doi:10.1029/2002GL015787.

Baker, D. N. (1984), Particle and field signatures of substorms in the near magnetotail, in *Magnetic Reconnection in Space and Laboratory Plasmas, Geophys. Monogr. Ser.*, vol. 30, edited by E. W. Hones Jr., pp. 193–202, AGU, Washington, D. C.

Baker, D. N., T. I. Pulkkinen, V. Angelopoulos, W. Baumjohann, and R. L. McPherron (1996), Neutral line model of substorms: Past results and present view, *J. Geophys. Res.*, *101*, 12,975–13,010.

Birn, J., and M. Hesse (1991), The substorm current wedge and field-aligned currents in MHD simulations of magnetotail reconnection, *J. Geophys. Res.*, *96*, 1611–1618.

Birn, J., M. Hesse, and K. Schindler (1996), MHD simulations of magnetotail dynamics, *J. Geophys. Res.*, *101*, 12,939–12,954.

Chang, T. (1999), The role of coarse-grained helicity and self-organized criticality in magnetotail dynamics, in *Magnetic Helicity in Space and Laboratory Plasmas*, edited by M. R. Brown, R. C. Canfield, and A. A. Pevtsov, pp. 277–284, AGU, Washington, D. C.

Coroniti, F. V., and C. F. Kennel (1973), Can the ionosphere regulate magnetospheric convection?, *J. Geophys. Res.*, *78*(16), 2837–2851, doi:10.1029/JA078i016p02837.

DeForest, S. E., and C. E. McIlwain (1971), Plasma clouds in the magnetosphere, *J. Geophys. Res.*, *76*, 3587–3611, doi:10.1029/JA076i016p03587.

El-Alaoui, M. (2001), Current disruption during November 24, 1996 substorm, *J. Geophys. Res.*, *106*, 6229–6245, doi:10.1029/1999JA000260.

El-Alaoui, M., R. L. Richard, M. Ashour-Abdalla, and M. W. Chen (2004), Low Mach number bow shock locations during a magnetic cloud event: Observations and magnetohydrodynamic simulations, *Geophys. Res. Lett.*, *31*, L03813, doi:10.1029/2003GL018788.

El-Alaoui, M., M. Ashour-Abdalla, J. M. Bosqued, and R. L. Richard (2008), Understanding magnetotail current sheet meso-scale structures using MHD simulations, *Adv. Space Res.*, *41*(10), 1630–1642, doi:10.1016/j.asr.2007.05.061.

Fedder, J. A., and J. G. Lyon (1995), The Earth's magnetosphere is 165 R_E long: Self-consistent currents, convection, magnetospheric structure, and processes for northward interplanetary magnetic field, *J. Geophys. Res.*, *100*, 3623–3635, doi:10.1029/94JA02633.

Frank, L. A., and J. B. Sigwarth (2000), Findings concerning the positions of substorm onsets with auroral images from the Polar spacecraft, *J. Geophys. Res.*, *105*, 12,747–12,761, doi:10.1029/1999JA000356. (Correction, *J. Geophys. Res.*, *105*, 18,919, doi:10.1029/2000JA900092.)

Frank, L. A., et al. (1995), Observations of plasmas and magnetic fields in Earth's distant magnetotail: Comparison with a global MHD model, *J. Geophys. Res.*, *100*, 19,177–19,190, doi:10.1029/95JA00571.

Hesse, M., and J. Birn (1991), On dipolarization and its relation to the substorm current wedge, *J. Geophys. Res.*, *96*, 19,417–19,426, doi:10.1029/91JA01953.

Hones, E. W., Jr., G. Paschmann, S. J. Bame, J. R. Asbridge, N. Sckopke, and K. Schindler (1978), Vortices in magnetospheric plasma flow, *Geophys. Res. Lett.*, *5*, 1059–1062, doi:10.1029/GL005i012p01059.

Hones, E. W., Jr., J. Birn, S. J. Bame, J. R. Asbridge, G. Paschmann, N. Sckopke, and G. Haerendel (1981), Further determination of the characteristics of magnetospheric plasma vortices with ISEE 1 and 2, *J. Geophys. Res.*, *86*, 814–820, doi:10.1029/JA086iA02p00814.

Hones, E. W., Jr., J. Birn, D. N. Baker, S. J. Bame, W. C. Feldman, D. J. McComas, R. D. Zwickl, J. A. Slavin, E. J. Smith, and B. T. Tsurutani (1984), Detailed examination of a plasmoid in the distant magnetotail with ISEE 3, *Geophys. Res. Lett.*, *11*, 1046–1049, doi:10.1029/GL011i010p01046.

Kistler, L. M., E. Möbius, W. Baumjohann, G. Paschmann, and D. C. Hamilton (1992), Pressure changes in the plasma sheet during substorm injections, *J. Geophys. Res.*, *97*, 2973–2983, doi:10.1029/91JA02802.

Knight, S. (1973), Parallel electric fields, *Planet. Space Sci.*, *21*, 741–750, doi:10.1016/0032-0633(73)90093-7.

Kokubun, S., and R. L. McPherron (1981), Substorm signatures at synchronous altitude, *J. Geophys. Res.*, *86*, 11,265–11,277, doi:10.1029/JA086iA13p11265.

Kokubun, S., T. Yamamoto, M. H. Acuña, K. Hayashi, K. Shiokawa, and H. Kawano (1994), The Geotail magnetic field experiment, *J. Geomagn. Geoelectr.*, *46*, 7–21.

Lopez, R. E., H. E. J. Koskinen, T. I. Pulkkinen, T. Bösinger, R. W. McEntire, and T. A. Potemra (1993), Simultaneous observations of the poleward expansion of substorm electrojet activity and the tailward expansion of current sheet disruption in the near-Earth magnetotail, *J. Geophys. Res.*, *98*, 9285–9295, doi:10.1029/92JA02401.

Lopez, R. E., C. C. Goodrich, M. Wilterberger, K. Papadopoulos, and J. G. Lyon (1998), Simulation of the March 9, 1995 substorm and initial comparison to data, in *Geospace Mass and Energy Flow: Results From the International Solar-Terrestrial Physics Program, Geophys. Monogr. Ser.*, vol. 104, edited by J. L. Horwitz, D. L. Gallagher, and W. K. Peterson, pp. 237–245, AGU, Washington, D. C.

Lui, A. T. Y. (1991), A synthesis of magnetospheric substorm models, *J. Geophys. Res.*, *96*, 1849–1856, doi:10.1029/90JA02430.

Lui, A. T. Y. (1996), Current disruption in the Earth's magnetosphere: Observations and models, *J. Geophys. Res.*, *101*, 13,067–13,088, doi:10.1029/96JA00079.

Lui, A. T. Y., R. E. Lopez, S. M. Krimigis, R. W. McEntire, L. J. Zanetti, and T. A. Potemra (1988), A case study of magnetotail current sheet disruption and diversion, *Geophys. Res. Lett.*, *15*, 721–724, doi:10.1029/GL015i007p00721.

Lui, A. T. Y., K. Liou, M. Nosé, S. Ohtani, D. J. Williams, T. Mukai, K. Tsuruda, and S. Kokubun (1999), Near-Earth dipolarization: Evidence for a non-MHD process, *Geophys. Res. Lett.*, *26*, 2905–2908, doi:10.1029/1999GL003620.

Lui, A. T. Y., et al. (2008), Determination of the substorm initiation region from a major conjunction interval of THEMIS satellites, *J. Geophys. Res.*, *113*, A00C04, doi:10.1029/2008JA013424.

Lyons, L. R., and J. C. Samson (1992), Formation of the stable auroral arc that intensifies at substorm onset, *Geophys. Res. Lett.*, *19*, 2171–2174, doi:10.1029/92GL02494.

McPherron, R. L. (1970), Growth phase of magnetospheric substorms, *J. Geophys. Res.*, *75*, 5592–5599, doi:10.1029/JA075i028p05592.

McPherron, R. L. (1979), Magnetospheric substorms, *Rev. Geophys.*, *17*, 657–681, doi:10.1029/RG017i004p00657.

McPherron, R. L., C. T. Russell, and M. P. Aubry (1973), Satellite studies of magnetospheric substorms on August 15, 1968: 9. Phenomenological model for substorms, *J. Geophys. Res.*, *78*, 3131–3149, doi:10.1029/JA078i016p03131.

Nagai, T. (1982), Observed magnetic substorm signatures at synchronous altitude, *J. Geophys. Res.*, *87*, 4405–4417, doi:10.1029/JA087iA06p04405.

Nagai, T., M. Fujimoto, Y. Saito, S. Machida, T. Terasawa, R. Nakamura, T. Yamamoto, T. Mukai, A. Nishida, and S. Kokubun (1998), Structure and dynamics of magnetic reconnection for substorm onsets with Geotail observations, *J. Geophys. Res.*, *103*, 4419–4440, doi:10.1029/97JA02190.

Peroomian, V., M. El-Alaoui, M. Ashour-Abdalla, and L. M. Zelenyi (2007), A comparison of solar wind and ionospheric plasma contributions to the September 24–25, 1998 magnetic storm, *J. Atmos. Sol. Terr. Phys.*, *69*, 212–222, doi:10.1016/j.jastp.2006.07.025.

Raeder, J., J. Berchem, and M. Ashour-Abdalla (1998), The Geospace environment modeling grand challenge: Results from a global Geospace circulation model, *J. Geophys. Res.*, *103*, 14,787–14,797, doi:10.1029/98JA00014.

Raeder, J., R. L. McPherron, L. A. Frank, S. Kokubun, G. Lu, T. Mukai, W. R. Paterson, J. B. Sigwarth, H. J. Singer, and J. A. Slavin (2001), Global simulation of the Geospace Environment Modeling substorm challenge event, *J. Geophys. Res.*, *106*, 381–395, doi:10.1029/2000JA000605.

Runov, A., et al. (2008), Multipoint in situ and ground-based observations during auroral intensifications, *J. Geophys. Res.*, *113*, A00C07, doi:10.1029/2008JA013493.

Sato, T., and T. Hayashi (1979), Externally driven magnetic reconnection and a powerful magnetic energy converter, *Phys. Fluids*, *22*, 1189–1202, doi:10.1063/1.862721.

Sergeev, V. A., V. Angelopoulos, D. G. Mitchell, and C. T. Russell (1995), In situ observations of magnetotail reconnection prior to the onset of a small substorm, *J. Geophys. Res.*, *100*, 19,121–19,133, doi:10.1029/95JA01471.

Sergeev, V. A., V. Angelopoulos, J. T. Gosling, C. A. Cattell, and C. T. Russell (1996), Detection of localized, plasma-depleted flux tubes or bubbles in the midtail plasma sheet, *J. Geophys. Res.*, *101*, 10,817–10,826, doi:10.1029/96JA00460.

Shiokawa, K., W. Baumjohann, and G. Haerendel (1997), Braking of high-speed flows in the near-Earth tail, *Geophys. Res. Lett.*, *24*, 1179–1182, doi:10.1029/97GL01062.

Spence, H. E., M. G. Kivelson, R. J. Walker, and D. J. McComas (1989), Magnetospheric plasma pressures in the midnight meridian: Observations from 2.5 to 35 R_E, *J. Geophys. Res.*, *94*, 5264–5272, doi:10.1029/JA094iA05p05264.

Takahashi, K., L. J. Zanetti, R. E. Lopez, R. W. McEntire, T. A. Potemra, and K. Yumoto (1987), Disruption of the magnetotail current sheet observed by AMPTE/CCE, *Geophys. Res. Lett.*, *14*, 1019–1022, doi:10.1029/GL014i010p01019.

Walker, R. J., T. Ogino, J. Raeder, and M. Ashour-Abdalla (1993), A global magnetohydrodynamic simulation of the magnetosphere when the inter-planetary magnetic field is southward: The onset of magnetotail recon-nection, *J. Geophys. Res.*, *98*, 17,235–17,249, doi:10.1029/93JA01321.

Walker, R. J., T. Ogino, and M. Ashour-Abdalla (1998), The response of the magnetosphere to a solar wind density pulse, in *Proceedings of the International Conference on Substorms: 4*, edited by S. Kokubun and Y. Kamide, pp. 527–530, Terra Sci., Tokyo.

Walker, R. J., M. Ashour-Abdalla, M. El-Alaoui, and F. V. Coroniti (2006), Magnetospheric convection during prolonged intervals with southward interplanetary magnetic field, *J. Geophys. Res.*, *111*, A10219, doi:10.1029/2005JA011541.

White, W. W., J. A. Schoendorf, K. D. Siebert, N. C. Maynard, D. R. Weimer, G. L. Wilson, B. U. Ö. Sonnerup, G. L. Siscoe, and G. M. Erickson (2001), MHD simulation of magnetospheric transport at the mesoscale, in *Space Weather*, *Geophys. Monogr. Ser.*, vol. 125, edited by P. Song, H. J. Singer, and G. L. Siscoe, pp. 229–240, AGU, Washington, D. C.

Winglee, R. M., A. T. Y. Lui, R. P. Lin, R. P. Lepping, S. Kokubun, G. Rostoker, and J. C. Samson (1998), Magnetospheric-ionospheric activity during an isolated substorm: A comparison between Wind/Geotail/IMP 8/CANOPUS observations and modeling, in *Geospace Mass and Energy Flow: Results From the International Solar-Terrestrial Physics Program*, *Geophys. Monogr. Ser.*, vol. 104, edited by J. L. Horwitz, D. L. Gallagher, and W. K. Peterson, pp. 181–191, AGU, Washington, D. C.

Yermolaev, Y. I., V. A. Sergeev, L. M. Zelenyi, A. A. Petrukovich, J.-A. Sauvaud, T. Mukai, and S. Kokubun (1999), Two spacecraft observation of plasma sheet convection jet during continuous external driving, *Geophys. Res. Lett.*, *26*, 177–180, doi:10.1029/1998GL900118.

Zhou, X.-Z., et al. (2009), Thin current sheet in the substorm late growth phase: Modeling of THEMIS observations, *J. Geophys. Res.*, *114*, A03223, doi:10.1029/2008JA013777.

———————————

V. Angelopoulos, M. Ashour-Abdalla, M. El-Alaoui, V. Peroomian, R. L. Richard, A. Runov, and R. J. Walker, Institute of Geophysics and Planetary Physics, University of California, 405 Hilgard Avenue, Los Angeles, CA 90095-1567, USA. (mostafa@igpp.ucla.edu)